7-1-2016

DESIGN, FABRICATION AND CHARACTERIZATION OF PHONONIC CRYSTALS IN MACRO AND MICRO SCALE

Mohammadhosein Ghasemi Baboly

Recommended Citation

Ghasemi Baboly, Mohammadhosein. "DESIGN, FABRICATION AND CHARACTERIZATION OF PHONONIC CRYSTALS IN MACRO AND MICRO SCALE." (2016). https://digitalrepository.unm.edu/me_etds/93

Mohammadhosein Ghasemi Baboly

Candidate

Mechanical Engineering

Department

This dissertation is approved, and it is acceptable in quality and form for publication:

Approved by the Dissertation Committee:

Zayd C. Leseman , Chairperson

Yu-Lin Shen

Ihab El-Kady

Mehmet F. Su

Mani Hossein-Zade

DESIGN, FABRICATION AND CHARACTERIZATION OF PHONONIC CRYSTALS IN MACRO AND MICRO SCALE

by

Mohammadhosein Ghasemi Baboly

DISSERTATION
Submitted in Partial Fulfillment of the
Requirements for the Degree of

Doctor of Philosophy

Engineering

Department of Mechanical Engineering
The University of New Mexico
Albuquerque, New Mexico

July 2016

إنَّ النَّفسَ

لَأمّارة بالسّوءِ إلّا ما رَحِمَ

ربّي

CONTENTS

LIST OF TABLES

LIST OF FIGURES

LIST OF ABBREVIATIONS AND ACRONYMS

Phononic Crystals	PnC
Photonic Crystals	PhC
Radio Frequency	RF
Microwave Wave	MW
Absolute BandGap	ABG
Surface acoustic wave	SAW
Bulk acoustic wave	BAW
Brulluin Zone	BZ
Finite Difference Time Domain	FDTD
Plane Wave Expansion	PWE
High Contrast Solid-Solid	HCSS

LIST OF APPENDICES

1 INTRODUCTION

Metamaterials have shown an excellent potential in many disciplines of science and technology in the last decade[1]. Metamaterials have generated a lot of interests due to their ability to manipulate over light as well as mechanical waves like sound waves and thermal properties which are not available in nature, so the physical properties of metamaterials is not essentially determined by chemical elements and bonds in the materials, but rather on the internal specific structures[2,3].

Periodic structures can have a large impact in thermal management[4]. Thermal energy in solid is transferred by electron and phonons. Thermal conductivity of dielectric materials and many semiconductors is determined mainly by the phonons since those materials don't have a large number of free carriers as metals. It is been demonstrated theoretically and experimentally that the thin films and two-dimensional (2D) phononic crystal, exhibited low thermal conductivity by modification of phononic band structure[5–7].

Phononic Crystals (PnCs) are well known for their great capabilities in controlling and modifying the flow of waves/particles especially in the domains of solid-state physics. PnCs are periodic composite structures comprised of two linear-elastic materials of varying mechanical properties. Structures of this type have the ability to inhibit the propagation of vibrational energy over certain ranges of frequencies forming bandgaps. These band gaps, which are known as “phononic” band gaps (PnCBGs), are ranges of frequencies in which elastic waves are prohibited from propagating in the medium and are either reflected or scattered upon impinging on such PnC structures, thus presence of a bandgap would reduce the flow of phonons and as the results thermal conductivity of a solid.

These bandgaps form due to Bragg scattering. In phononic crystals, mismatch between the acoustic velocity and impedance of the two materials results in a phononic bandgap. However, in phononic crystals, the velocity and impedance are related through material density, and therefore can be independently controlled[8,9].

The applications of bandgap and phononic crystal devices stimulated a renewed interest in the propagation of elastic waves composite structures. Besides, PnC structures can be used to confine, guide and manipulate mechanical vibrations if a defect is introduced into the structure. Wave behavior in defected phononic crystal structures in point and line defects have also been considered[10]. Kafesaki numerically calculated the trasmittivity of acoustic waves through a defected PnC (wave guide) by removing one row of cylinders[11].

In 1979 Narayanamurati et al. reported the first successfully observation of a periodic structure made of a GaAs/AlGaAs super-lattice used to control the propagation of high frequency phonons. Nowadays supper lattice is considered as one-dimensional phononic crystals[12]. The first two-dimensional and three dimensional phononic crystals were introduced at early 1990s. Sigalas demonstrated the existence of absolute band gaps in the band structure of acoustic and elastic waves in 3-D structures composed of sphere arranged periodically within host materials[13]. F. R. Montero de Espinosa et al. showed the first experimentally observed bandgap in solid-solid PnCs for longitudinal waves for a two dimensional PnC composed of an aluminum plate with a square array of cylindrical holes filled with mercury[14].

Vasseur et al reported the first experimental and theoretical study of an absolute bandgap in two dimensional binary solid-solid composite media composed of arrays of Duralumin cylindrical inclusions embedded in an epoxy resin matrix. They reported the experimental transmission spectrum and theoretical band structure of two periodic arrays of cylinders arranged in a square lattice and on a centered rectangular network[15].

Outstanding characteristics of Phononic crystal devices with sizes of the order of ~mm or less such as surface acoustic wave (SAW) filters and devices have opened a new horizon to the wireless communication devices and sensors industry[16–18].

Moreover, some other quasi particles such as photons, show a similar behaviour. Photonic crystals (PhCs) are periodic structures with variation in their optical properties that affects the motion of photons. They have already shown their great capabilities in controlling the flow of optical waves or their dual particles (i.e., photons) using PhCBGs [19]. Various novel Photonic Crystal (PhCs) devices were introduced that were using PhCs Bandgaps including PhC fibers[20], waveguides[21], and resonators[22], which have shown great performances. The same ideas are applied to phonons and acoustic (or elastic) waves. Because of the increasing applications of wireless communication devices and sensors, there has been significant effort to develop Mechanically-Vibrating devices[23,24].

Curie brothers had introduced Piezo-electricity effect in 1880. Mechanically vibrating elements such as quartz crystals have been widely used for sensing devices and telecommunication applications [16,25,26]. These devices were also used for high quality filters and various sensing elements. These elements were implemented for different variety of applications in SAW devices, which have many applications, especially in communications, sensing and radar systems.

several theoretical[27–29] and experimental[30,31] studies were performed to prove the existence of PnCBGs, and various devices were fabricated utilizing techniques from the well-established microelectronics fabrication industry[32]. Early PnCs and acoustic metamaterials research on spectral properties focused on frequencies in the sonic and ultrasonic ranges[10].

A number of modelling techniques such as finite difference time domain(FDTD)[8], boundary element methods (BEM)[33], global matrix approaches[34], plane wave expansion (PWE)[35], finite element (FE) modeling[36] have been utilized to predict the elastic transmission and characteristics of elastic waves in PnCs,. Among all of these methods, three major techniques, FDTD, PWE, and FE method have been developed and widely used due to their great performance.

The FDTD method has long been used to solve wave propagation problems in the fields of acoustics and electromagnetism. This is because of simplicity and the ability to solve large problems, straightforward parallelization, and possibility of simulating propagation problems involving a wide frequency range in a single run. In addition, one of the main advantages of this method over other computation techniques is the fact that it does not involve any matrix inversion however it is not capable of calculating modes and band diagram of the periodic structures.

PWE is also one of the most studied methods and a very reliable technique. This method allows the computation of Eigen Frequencies for Photonic/Phononic crystals to any prescribed accuracy, equal with computing time[35,37]. PWE has proved to be the reference method for the calculation of band gaps in PhCs[38]. Since the numerical precision of the PWE is limited by the number of terms kept in the Fourier expansions, is that PWE method has major drawbacks pertaining to the convergence difficulties especially when dealing with high contrast solid-solid (HCSS) PnCs. The conventional fix is to use an ever-increasing number of reciprocal lattice vectors (RLVs), which ultimately translates into large computational demands[39].

FEM (Finite Element Method) is one of the most effective methods used in various fields of engineering for solving many partial differential equations. Although FE method has the advantage in modelling the complicated electrical and mechanical boundary conditions, it is a time-consuming technique in simulating wave propagation problem, in which the size of the element is of the order of the wavelength. While FDTD and PWE methods are versatile methods that can be used to solve a large class of general problems, they are not specially optimized for calculation of the modes and the band structure of the periodic structures. FEM is relatively faster and more accurate than the other methods[40].

Experiments and numerical analyses have been performed on structures comprised of Si[41], SiC[42], and SiO_2[43] as the matrix material and air and tungsten as the inclusion material.

More recently, there have been demonstrations that a hexagonal lattice of scattering inclusions provides a wider bandgap than other lattice types such as a square lattice. However, the thickness needed to generate the wider bandgap is considerable thicker than that for the square lattice[44]. This complicates excitement of mechanical waves in the PnC with surface-mounted interdigitated transducers (IDTs), which are commonly used for experimentation[36]. This has led researchers to design more exotic unit-cell structures, such as crosses and snowflakes, in an effort to reach wider bandgaps and attain better confinement in defect structures[45].

AlN has been commonly used as the material for IDTs, but not as commonly for the PnC's matrix material[42,46]. Recently AlN have been under attention of some researchers due to its piezoelectric nature AlN and compatibility with most IC manufacturing processes it is a good candidate for the matrix material of PnCs. The added benefit of this material is that a monolithic device can be manufactured that includes the PnC and the IDTs thereby reducing insertion losses when compared to implementations with Si[47].

Different classes of PnCs have been introduced recently by inverting the acoustic velocity distribution in the unit cell, where high acoustic velocity materials such as silicon or aluminum nitride are in the center of the unit cell and surrounded by a low acoustic velocity medium, i.e. cermet topology [48,49] . For a square-lattice PnC, the material in the center is connected to four thin tethers.

Many practical non-destructive evaluation (NDE) techniques have been developed for detecting wave propagation problems[50,51]. Recently, piezoelectric actuators and sensors have been widely used in damage detection of various structures to excite the surface wave devices and some consumer areas such as pagers, mobile phone, and sensors[52–54]. The advantage of piezoelectricity can be made useful in exciting elastic waves using electrical signal input. Both requirements of convenience and precision in wave excitations are satisfied using this mode of actuation. In addition, piezoelectric sensor is much more consistent and reliable than conventional strain gauge to determine damage location, since piezoelectric sensors are self-powered[55].

Though phononic crystals were proposed two decades ago[56], recent interest in their applications in higher frequency ranges have grown as portable electronics require ever-greater levels of energy-saving technologies[57]. The potential to passively filter noise from high-frequency signals is appealing because eliminating even the miniscule power drain of active filters can help manufacturers extend the battery life of their products and some other advantages in the incredibly competitive portable electronics marketplace.

In the field of designing macro PnCs, different researchers have attempted to design different waveguides and resonators. X. G. Zhao et al used Piezoelectric transducers to actuate waves and detect signal on a defected steel plates[58]. In addition to application of the wave guides in telecommunication industry, guided waves have shown the promising capability for detecting many defects that occur in pipe or plate structures that are not easily and efficiently detected by other means[59].

In addition, it is important to study the origin of bandgap formation. The appearance and subsequent disappearance of a bandgap as the dimension of the PnCs varies is attributed to the different deformations possible for this 3D structure. All of the works on PnC devices utilized numerical and experimental implementation to observe bang gap and none of them has studied the origin of the bandgap. This could be done by assuming phononic crystals as a coupled oscillation system and observing mode shapes and mode rate as the dimensions of PnC change.

As was mentioned, because of the PnCs' ability in phonon manipulation to trap and guide mechanical energy, PnC slabs are outstanding candidates for the application of integrated wireless devices. Wave guiding is one of the most fundamental functionalities of the envisioned PnC-based integrated devices. In the recent years most of the experimental works are done to show the bandgap or design a resonator but no one has designed a single mode waveguide yet. There are a few numerical and experimental works were performed to show guiding mode. The studies that are available have leaky modes and guide multiple modes in the bandgap[9,60].

In this study the author will attempt to characterize macro PnC devices made of Aluminum such as PnC, cavity, and some other devices including single mode waveguides, 90˚bend and splitters that have not been experimentally demonstrated. Also micro PnCs are fabricated and tested using aluminum nitride(AlN). In addition the aim is to study the mode behaviour by the mode shape analysis and investigate the provenance of bandgap formation. While the implementation of the PnC devices in this work has been done in Aluminum and AlN, most of the results and ideas reported here can be used for other materials such as Si, SiC, etc.

This chapter provides an overview of the fundamentals, application and progress of PnC structures and SAW devices. In Chapter 2, the two major numerical simulation tools are introduced in this area for the analysis of elastic and acoustic wave propagation. These methods are basic and fundamental methods in designing and characterizing PnC structures and devices and each have their own advantages and disadvantages, Also the experimental setup for Macro PnCs will be explained and numerical and experimental results For variety of PnC devices will be presented and discussed.

In Chapter 3, the developed methods for characterizing PnCs will be utilized to design and fabrication of extremely high frequency Micro PnCs and resonators. The possibility of obtaining wide bandgaps in PnC structures at higher frequencies that are compatible with micro/nano fabrication technology by explaining each fabrication steps. Also characterization setup is demonstrated by utilizing a network analyzer and using that to perform the experiments.

In Chapter 4, a very necessary study is performed to optimize the bandgap. One of the last pieces of PnCs puzzle is the ways to optimize the bandgap width and shedding light on the origin of the PnCs bandgaps, and finally in Chapter 5 for the very first time I showed the importance of mode shape and experimental demonstration of the mode shapes for cavity and waveguide. Conclusion and future work is provided in chapter 6.

2 DESIGN, FABRICATION AND EXPERIMENTATION OF MACRO PNC DEVICES

2.1 Overview:

In this chapter, my main scope is to design and implement Macro PnC devices operating at kHz frequency ranges. Five main planar PnC devices made totally of Al are considered in this chapter. The periodicity and thickness in these PnC structures is in mm order. This will ensure the low-cost fabrication and compatibility transducers out in the market.

This study of phononic crystals is being performed to characterize the bandgap attenuation effects of different configurations of filling fraction and packing of the inclusions. The scope of this study is restricted to macro-scale crystals operating in the kilohertz (kHz) range, as they are significantly easier and less expensive to fabricate. One of the traditional ways to test these devices is to launch and receive mechanical waves using piezoelectric transducers. The analysis of the macro-scale crystals' effects can then be applied to the micro-scale where crystals operate in the mega-, giga-, and terahertz range.

In Section 2.2, theory and governing equations for mechanical wave in solid media and Reasons for bandgap existence are explained and discussed in details. Equation of motion is simplified for elastic waves are derived and simplified.

In Section 2.3, Finite Element Analysis for such PnC structures for controlling and characterizing SAWs will be explained in detail. Modelling PnCs for the desired operating range was performed with COMSOL Multiphysics. Different FEM modelling techniques will be discussed for different PnC devices.

In Section 2.4, and experimental platform that was designed for characterizing the attenuation of the bandgaps for different devices will be introduced. Different components of the setup will be explained.

Finally in section 2.5, experimental and numerical results for all devices will be shown and It will be shown that large PnCBGs can be obtained in PnC SAW structures and used for some applications. Also wave Bending and splitting will be experimentally demonstrated through a defected structure.

2.2 Theory:

In this section the equation of motion for an isotropic section is derived for particular displacement. Two types of waves so called longitudinal and transverse could be propagated through an unbounded solid material. The equation of motion in terms of stress and strain in a 1-D solid media could be written as:

$$\rho\frac{\partial^2 u}{\partial t^2}=(\lambda+2\mu)\frac{\partial^2 u}{\partial x^2} \tag{2-1}$$

Where λ and μ are Lame's Constants and the relation between them and elastic modulus (E) is:

$$E=\frac{\mu(3\lambda+2\mu)}{\lambda+\mu} \tag{2-2}$$

In the first glace it can be conclude that $\frac{E}{\rho}$ plays an important role in the wave propagation motion. When an elastic wave of either type reaches the interface 2 different media, in general, two waves are generated. One of them will propagate through the second media and the second one reflects back. There are 4 boundary conditions to be satisfied and they are :

i. u_a=u_b (normal displacement)
ii. v_a=v_b and w_a=w_b (tangential displacement)
iii. $\sigma_{xx(a)}$ =$\sigma_{xx(b)}$ (Normal stress)
iv. $\sigma_{yx(a)}$ =$\sigma_{yx(b)}$ and $\sigma_{zx(a)}$ =$\sigma_{zx(b)}$ (tangential stress)

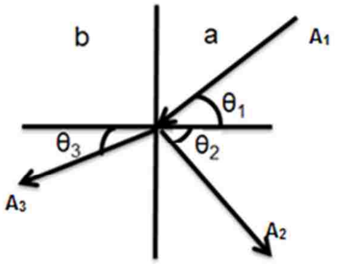

Substituting 3 and 4 in terms of displacement we get:

$$A_2=\frac{A_1(\rho_b c_3-\rho_a c_1)}{\rho_b c_3+\rho_a c_1} \tag{2-3}$$

$$A_3=\frac{A_1(2\rho_a c_1)}{\rho_b c_3+\rho_a c_1} \tag{2-4}$$

Thus the amplitude of reflected wave depends on the $\rho_b c_3-\rho_a c_1$. So if the product of density and velocity is the same for 2 media there will be no reflection. This product is known as *characteristic impedance(Z)*[61].

Substituting c in the characteristic impedance equation we get: $\boldsymbol{Z=\rho c=\sqrt{E\rho}}$

So having Eq. 2-3 and Eq. 2-4 the most important factor for the reflection is:

$$A_2 = \frac{A_1(\rho_b c_3 - \rho_a c_1)}{\rho_b c_3 + \rho_a c_1} = \frac{A_1(Z_2 - Z_1)}{Z_2 + Z_1} \tag{2-5}$$

There is <u>NO</u> bandgap, if the materials are same or if they are perfectly impedance matched. In order to get maximum reflection we should maximize the impedance mismatch. This parameter is the key to widen the band gap and modify the gap to midgap ratio. The higher the impedance mismatch is the wider bandgap could be obtained.

2.3 Finite Element Model

COMSOL Multiphysics Finite Element Analysis (FEA) software was also used to simulate the performance of the PnC devices. Eigen Frequency analysis was performed to solve some of the wave propagation problems in PnC structures. The Eigen frequency analysis was verified, by performing a frequency domain analysis and it matched with band diagram. Since all the structures are large and have translational symmetry in at least one direction, periodic boundary conditions are used to limit the simulation to only one period and save computational time in that direction. The emphasis of the finite element model was on predicting the location of the bandgap for PnC and cavity and guided mode on other PnC devices. The location of the bandgap however dependents on the material properties such as stiffness/compliance matrix and density of host and inclusion materials, and those are well documented in literature . Therefore an accurate Eigen frequency analysis as well as frequency domain response simulation is possible and was conducted.

To study the behaviour of PnCs in the Eigen frequency domain, one period of the PnC devices and their important geometrical parameters are modelled and periodic boundary conditions are applied in x and y direction. Figure 2 shows the geometry of the structure in simulation view. The PnC structure used in this work is made by embedding a simple cubic array of cylindrical holes in an Al slab. The spacing between the closest holes (a) is equal to 8mm, the radius of holes (r/a) is 0.48 , and the thickness of the slab (t/a) is 4mm. 3D simulation was employed and all possible modes of propagation were considered, i.e. in-plane, out-of-plane transverse, and longitudinal modes. Using the band diagrams, the primary bandgap widths can be determined, where the bandgap is defined as the frequency range for which no modes can propagate over the entire irreducible Brillouin zone. The structure is modelled as a stress-free boundary condition in the x, y and z directions. (Appendix 1)

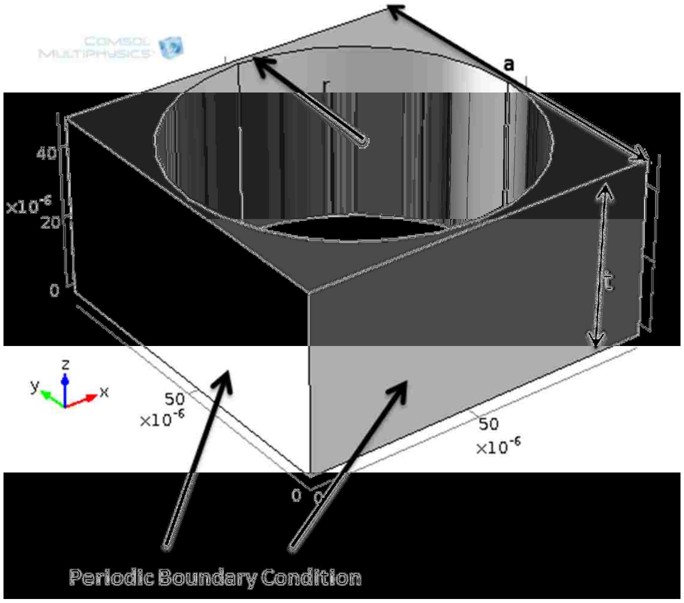

Figure 2.1: PnC formed from a cubic array of cylindrical air holes in an Al matrix with r/a = 0.48, t/a = 0.5.

Resonator designed in this work is made by eliminating one period (1 row) of holes from the PC structure to form a line-defect cavity as shown in Figure 2.2.

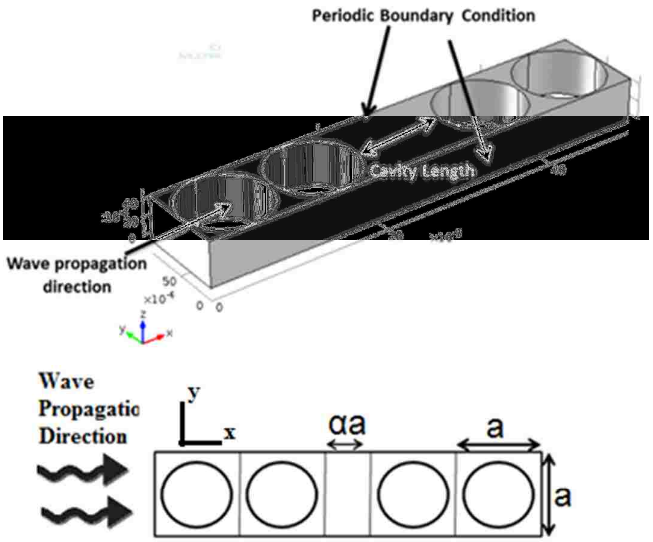

Figure 2.2: Eigen frequency model (top) and schematic (bottom) of PnC resonator design.

The acoustic waves with frequencies within the ABG can be trapped between the two PnC regions forming a resonator.

In addition a single mode waveguides (Figure 2.3) is designed as well as 90˚ bend/T and Y splitters by introducing a line defect to the PnC. Those devices show the guiding and the bending of acoustic waves in highly confined waveguides from a periodic two-dimensional lattice of aluminum-air PnC.

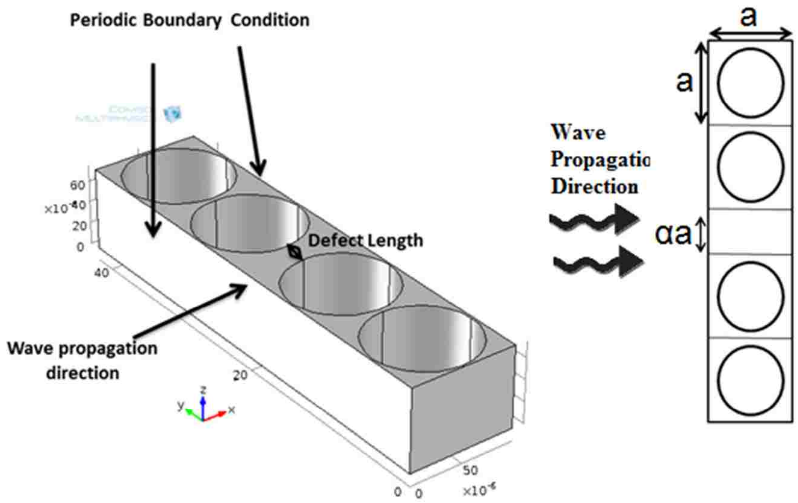

Figure 2.3: Schematic (right) and Eigen frequency model (left) of PnC waveguide design.

Eigen Frequency analysis is as very fast and accurate way of studying the behavior of PnC structures but one of the disadvantages is, it is hard to use it for large structures such as 90^o bend and splitters. In contrast, for frequency domain analysis is a very neat way to analyse them, in COMSOL. Perfectly Matched Layers (PML) is utilized to have zero reflection from the PnC interface boundaries. Periodic boundary conditions were employed along the y-direction to model an infinitely periodic structure and reduce the computational time. . Longitudinal waves are launched into the PnC by applying harmonic deformation of the nodes on the whole surface of left domain and then the transmission is attained by determining the amplitude of the incident wave to the PnC in Domain 1, and the amplitude of the transmitted waves through the PnC in Domain 2. Figure 2.4 shows the frequency domain analysis for 90˚bend T and splitter.

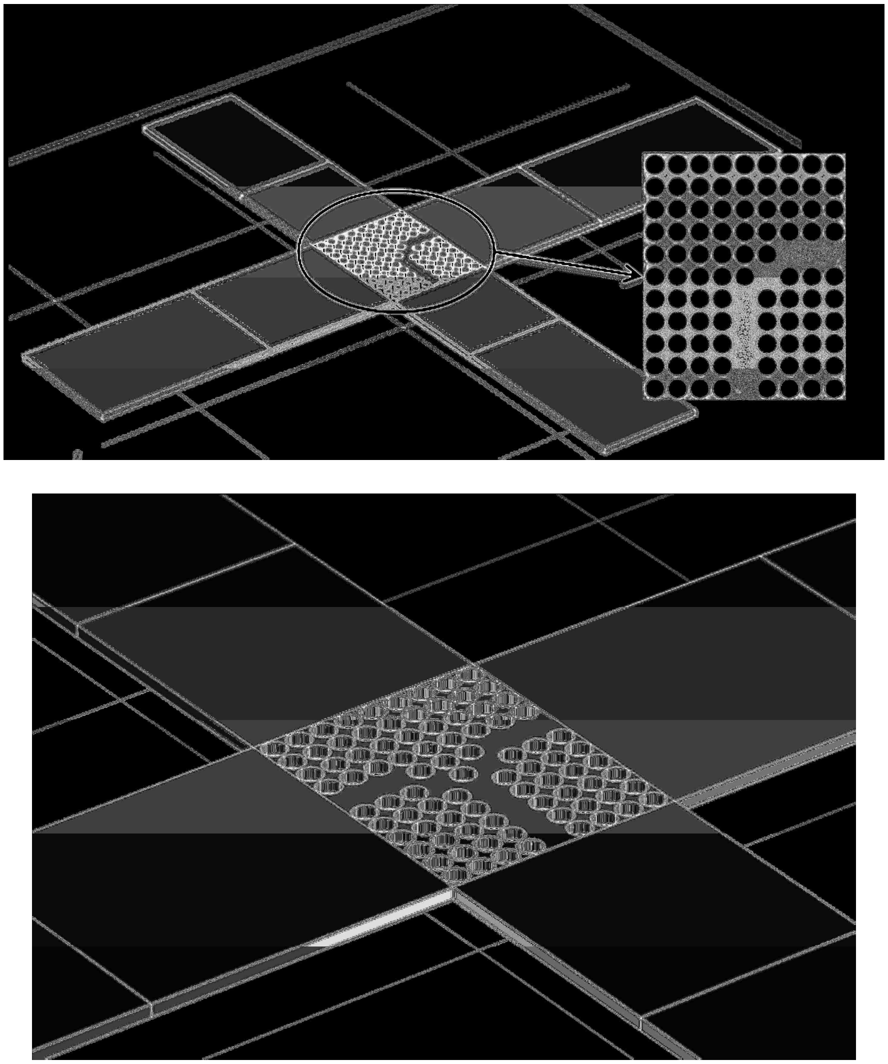

Figure 2.4: Frequency domain Analysis view for 90° Bend and T-Splitter.

Frequency domain analysis is a time consuming method and its convergence problem is prevalent because in simulating mechanical wave propagation problem the size of the element should be of the order of the wavelength.

In this structure, Al was used as host material with air inclusions and the spacing between the closest holes (a) is equal to 8 mm, the radius of holes (r) is around 3.88 mm ($r/a = 0.485$), and the thickness of the slab (d) is 4 mm. The FEM simulated dispersion relationship is presented in Fig. 7. The FEM result displays a complete frequency band gap centred about 176 kHz and ranging from 150 kHz to 202 kHz, which corresponds to a gap-to-midgap ratio of ~29%.

2.4 Design criteria and Modelling

2.4.1 Experimental Setup

In order to design the test platform such that it is capable of providing high-quality test signals and optimally capturing the transmitted signal, it is essential to understand the base-level attenuation of the device under test as well as the band-attenuation expected from the PnC configuration.

The test platform shown in Figure 6 is designed such that it is capable of providing up to several millivolts accuracy. Although the signal output required for the PnC test specimens is much lower but the specifications are set purposefully much higher than the requirement to allow for some margin to work with other materials if required and also other purposes such as other S parameters measurement, damping factor measurement, structural health monitoring. On test platforms used for testing PnC devices it is imperative that the mechanical waves will be transmitted from piezo to the PnC slab and will be captured by the piezo crystal on the other side and will be displayed on the oscilloscope. Listed below are some of the parametric trends for PnC devices:

1. The natural frequency for a system with masses and springs is proportional to the square root of the ratio of the stiffness to mass.
2. Increasing the unit cell size will result in lower frequency bandgap.
3. The band gap width is proportional to air filling fraction.

4. Maximum output displacement and voltage increases linearly with the input voltage and it is limited by piezoelectric transducer specification. Higher input voltages will provide better output signal as the wave amplitude is stronger but from the other side will give noisier signals with more reflection due to the impedance mismatch between transducers and amplifier.
5. If the distance between piezo actuators and PnC is an integer coefficient of the lattice constant, will make create standing waves.

Based on the above specifications, finite element models were developed for the crystals and the predicted band-gap was observed. A solid-Air PnC will be made of Aluminum specimen that is 14cm long, 3-4 cm wide, and 4 mm thick. Testing will take place at room temperature and based on the simulation crystals must display an attenuation band-gap in the 150 kHz to 200 kHz range.

Then a test platform was design, fabricated, and characterized to perform frequency response testing. The test platform will include signal generator, oscilloscope, signal conditioning filter, and crystal isolation platform. The incident wave will be excited in the phononic crystal by a piezoelectric crystal mounted on one end, and the transmitted wave will be recorded by a second piezoelectric crystal mounted on the opposite end and after passing a butterworth filter data will be collected by an oscilloscope. Then Fabrication of macro-scale phononic crystals from aluminum for following devices slab, phononic crystal devices such as, PnC cavity, and waveguide,90°bend, T-splitter and Y-splitter.

After filtering all noise frequencies and recording neat and clean data, a custom MATLAB script will be written for Fast Fourier Transformation analysis of output signals to ensure the accuracy of output frequency. Also LabView program is used to automize the setup. A custom LabView script was written to automate frequency response testing of crystals by controlling signal generator and oscilloscope. Then having verified the setup tested for different devices and at different frequency ranges the following experiments are performed:

a. Characterize the base attenuation of the slab.
b. Characterize the attenuation band gap for the Phononic crystals.
c. Characterize the attenuation band gap(s) for the crystal with cavity.
d. Characterize the attenuation band gap for the waveguide and other wave guiding devices such as 90°bend, T-splitter and Y-splitter.
e. Investigating the band gap's origin by studying the mode-shapes and mode rates.

For this study, the author intends to build a platform for testing macro-PnC's that will work for all combinations of slab, crystal, cavity, and waveguide configurations. This platform provides isolation for the PnCs to maximize wave transfer and minimize energy dissipation through interaction with the platform, as well as signal conditioning to eliminate higher-frequency noise generated by oscillation modes of the crystal. Test automation allows for large data sets to be easily and consistently obtained for the crystals.

It is also necessary to minimize the standing waves through the crystal. It can arise in a stationary medium as a result of interference between two waves traveling in opposite directions. In the second case, for waves of equal amplitude traveling in opposing directions, there is on average no net propagation of energy.

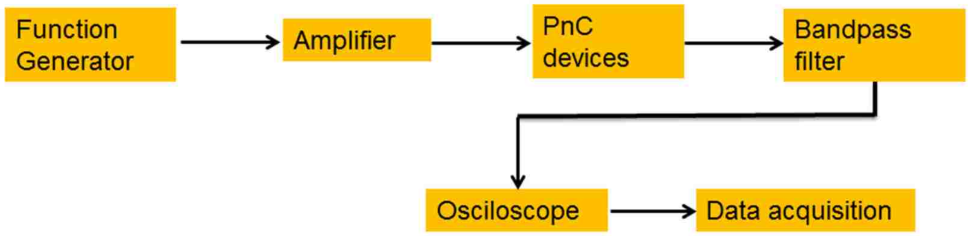

Figure 2.5 Schematic of setup used for Macro PnC test.

The schematic of the PnC device, testing platform proposed for this work is shown in Figure 2.5. The system is composed of three distinct features; a) Function Generator and oscilloscope b) the Aluminum PnC test specimen and c) Piezo-electric transducer. The test specimen is attached at one end to 4 plastic pillars to avoid wave transmission to the substrate. Piezoelectric transducers will be used to launch and receive motions and convert it to voltage signal and oscilloscope and function generator will be used to generate the desired wave at any frequency and receive signals from piezoelectric transducers and display it.

2.4.2 Device Fabrication and test platform

The crystals are fabricated from solid aluminum blocks. Using a computer-aided milling machine, slabs are cut from 99% pure aluminum and are dimensioned to exactly 14× 3.2× 0.4 cm with a tolerance of 0.001 of an inch. Inclusions are created by the same machine, in a rectangular packing pattern (simple cubic unit cell), with radius to lattice constant ratio (r/a) of 0.48 and center-to-center distances of 8 mm. For the defected structures two periods of PC holes are placed on each side of the PC cavity and waveguide to provide enough confinement for the trapped modes in the PnCBG. The line defect on the cavity and waveguide are surrounded by two periods of holes on each side, as shown in Figure 2.6. Inset provides PnC device consist of 4 rows and 5 columns.

The test platform is composed of several distinct parts: a) signal generation b) the phononic crystal c) isolation and signal conditioning d) data acquisition system and e) automation.

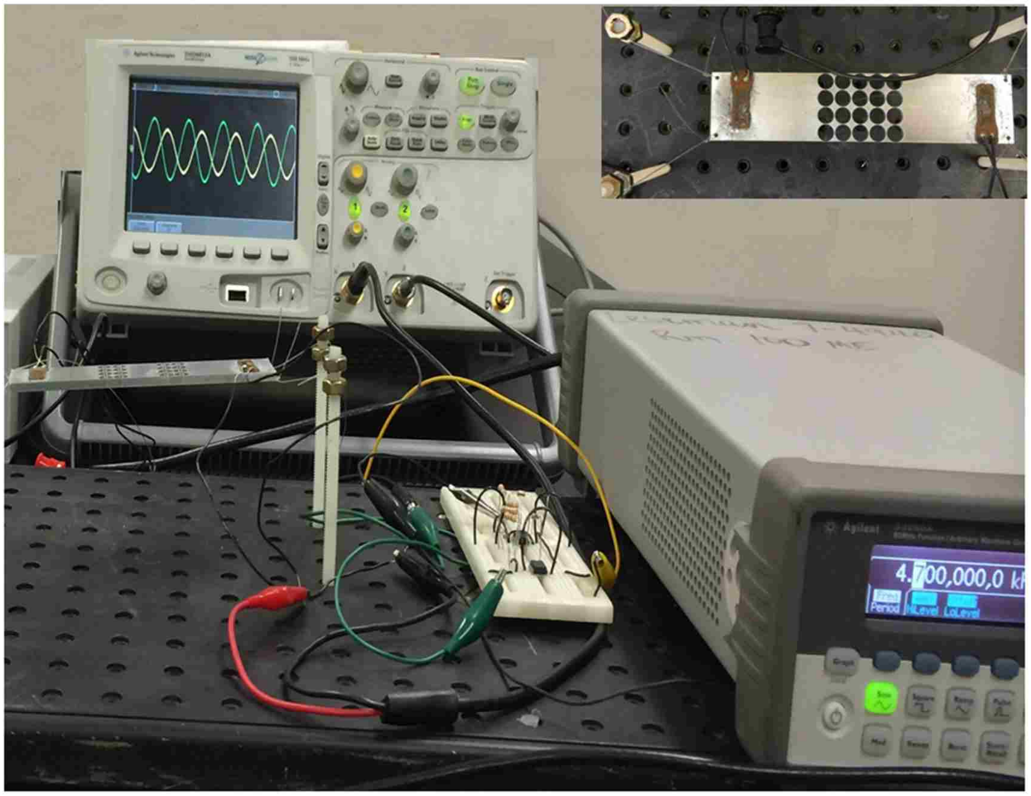

Figure 2.6 Test platform for testing the macro PnC devices.

Signal generation provided by a frequency generator, which provides a nominal 10 Vpp sine wave at desired frequencies. The phononic crystal is constructed from an aluminum block, with an inclusion pattern drilled through the plate, and two piezo-electric crystals bonded to opposite ends. Isolation is obtained by fixing the crystal in middle of the air making a suspended bridge. This achieved by tying the crystal to four semi-rigid pillars affixed to the test bed. Signal conditioning is provided by an impedance-matched 3rd-order Butterworth filter.

Due to the ease of excitation and application, piezoelectric crystals are attached to the completed phononic crystal with cyanoacrylate adhesive. The piezo crystals are oriented parallel to each other, flush with the outside edge of the same top surface. Lead wires are soldered onto the piezo crystals to allow them to connect to the function generator and filter.

Data acquisition is conducted by an oscilloscope, which samples both the transmitted signal as well as the original signal. It stores five thousands samples of each wave. Automation is managed by a custom Labview script, which drives both the function generator and the oscilloscope.

2.4.3 Frequency Measurement Methodology

The test signal is a nominally 10 Vpp sine wave. Frequencies from 100 kHz to 300kHz are tested, with a step size of 1 kHz. The transmitted wave has amplitude ranging between 20 and 200 mVpp, and is of the same frequency as the transmitted wave. The amplitude and frequency of the transmitted wave are calculated with MATLAB, and the results are normalized to the transmission of the slab. The resulting attenuations are plotted on a transmission-frequency graph, and the band-gap is defined as the region showing an attenuation of -10 dB or lower. The output frequency is noisy and the noise should be filtered. A 3rd order butter worth filter is made to filter the noise signal and attain clean signal.

2.4.4 Results and discussion

In this section numerical and experimental results will be presented for PnC devices. Before presenting the results the material chosen for PnCs and the lattice type is discussed in details.

- **Materials:**

  Before starting any kind of design a good set of host and inclusion materials should be chosen. Different types of materials were simulated and finally aluminum-air was chosen as the PnC. The results are shown in the table 3.1 for all of the all parameters are kept the same and gap-to-midgap ratio was compared. The lattice type is square lattice with circular inclusions.

Materials	impedance(kg/m^{2}s)	Midgap frequency (MHz)	Gap to midgap ratio
Lead	13.50×10^6	3.845	34.07
Platinum	60.03×10^6	9.085	32.03
Aluminum	13.74×10^6	16.55	30.93
Copper	32.79×10^6	11.9	30.75
Nickel	44.18×10^6	16.16	29.57
Tungsten	89.17×10^6	15.05	28.5
Steel	34.56×10^6	14.37	28.25
Epoxy	2.03×10^6	4.92	25.20
SiO_2	12.80×10^6	18.59	24.95

Table 2.1 table of materials with bandgaps. For each set of materials lattice constant is 100 um and r/a=0.48 and t/a=0.5

As can be seen aluminum shows a large bandgap among all of those materials. There are other materials that could be picked as well but aluminum (Al) is a dominant material in any machine shop. It is easy to machine an in contrast with steel. Aluminum is way cheaper than some other metals like platinum or gold and more importantly it is not toxic like lead.

- Lattice:

  5 types of lattices (e.g. square, rectangular, centered rectangular, triangular and honey comb) are been examined and simulated and square lattice provides the widest bandgap for thinner Al-air PnCs. Thinner slabs are preferable because it is easier to actuate them with piezoelectric transducer used in this work. Figure 2.7 shows a summary of bandgaps for different lattices.

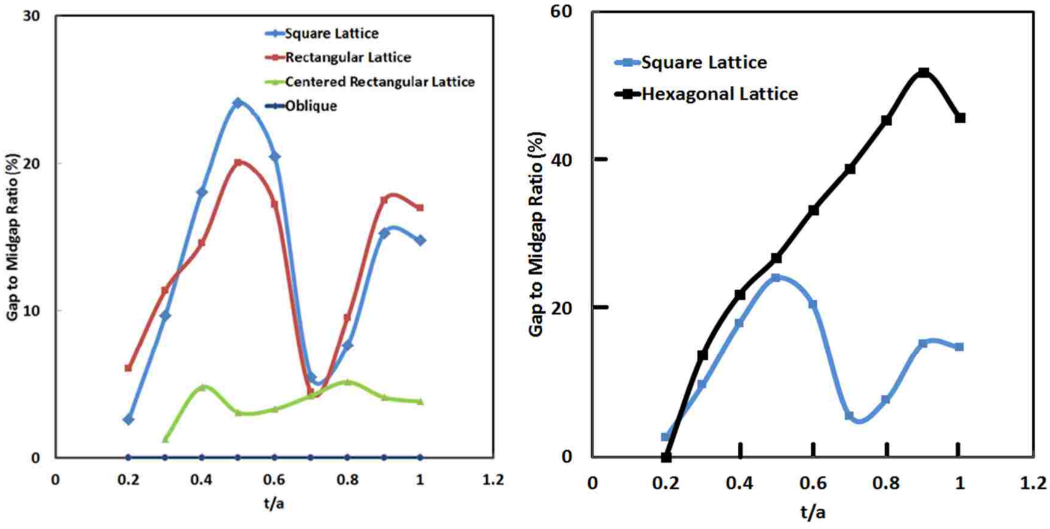

(a) (b)

Figure 2.7 Comparison between different lattice types

It is clear square lattice has a higher gap-to-midgap ratio for all thicknesses among all lattices except hexagonal. (figure 2.7a) Although hexagonal lattice shows a wide bandgap for thicker slabs the square lattice, there is not much difference between hexagonal and square lattice for thinner structures.(figure 2.7b) Also another reason for selecting the square lattice was it is easier to machine and the structure is simpler.

2.4.4.1 PnC

In this structure, Al was used as host material with air inclusions and the spacing between the closest holes (a) is equal to 8 mm, the radius of holes (r) is 3.88 mm($r/a = 0.485$), and the thickness of the slab (d) is 4 mm. The FEM simulated dispersion relationship is presented in Figure 2.8. The FEM result displays a complete frequency band gap centred about 176 kHz and ranging from 150 kHz to 202 kHz, which corresponds to a gap-to-midgap ratio of ~29%.

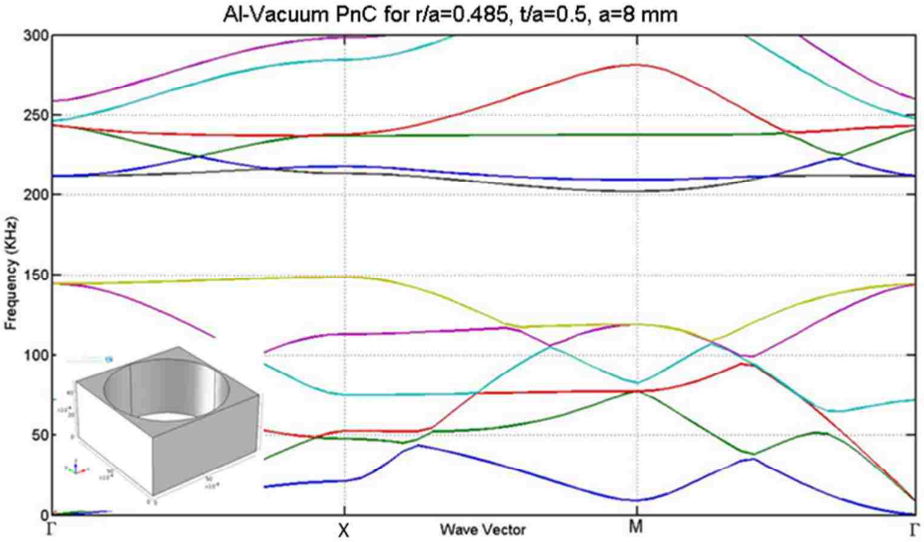

Figure 2.8 Calculated acoustic band diagram of a PnC formed from a cubic array of cylindrical air holes in an Al matrix with r/a = 0.48, t/a = 0.5, Calculated Acoustic BandGap (ABG) is between 150-202 kHz.

In addition, the transmission spectrum of PnCs was calculated using frequency domain analysis and the bandgap is depicted in Figure 2.9. The frequency domain analysis is in an excellent agreement with the Eigen Frequency (dispersion relation). It is worth to note that in the Eigen Frequency Analysis because of the periodic boundary condition structure is assumed infinite by infinite but for frequency domain analysis the PnC is a finite structure and the band gap is 2-3% shifted.

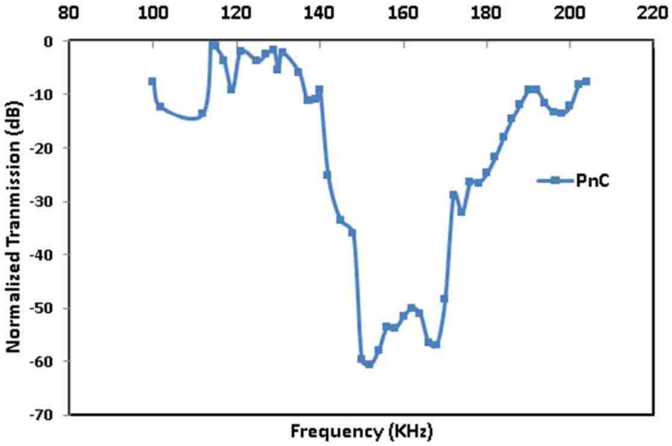

Figure 2.9 Transmission spectrum based on 3D frequency domain FEM analysis. The band gap is between 140 to 195 kHz.

The PnC display a bandgap in the 140 kHz to 185 kHz range (Figure 2.10). The bandgap obtained experimentally is roughly 3-5% lower than those obtain numerically.

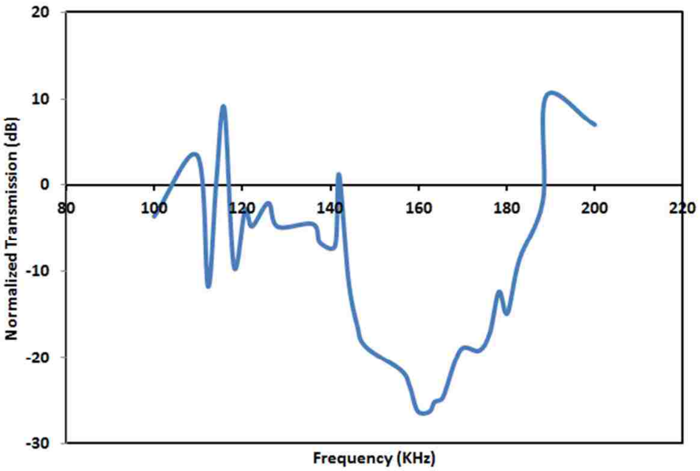

Figure 2.10 Experimental transmission results of a PnC formed from a cubic array of Al-air PnC with r/a = 0.48, t/a = 0.5. It displays a bandgap between 140 to 185 kHz.

This difference is likely due to fabrication tolerances and the difference in material properties of Al sample tested and FEM material library also the fact that the experiment was conducted for aluminum-air holes (solid-air) and FEM aluminum-vacuum PnCs were modelled. The measurements were all done at room temperature and atmospheric pressure.

2.4.4.2 Cavity

As was previously mentioned PnCs have the great possibility of confining and guiding of mechanical energy with low loss using Phononic Crystal slabs with bandgaps. Therefore, PnC slabs are one of the best choices for wireless devices, at any frequency range, especially for high frequency applications, in which unit cell dimensions is relatively small (~µm); an result in high frequency confinement. However, until now there had been very few theoretical and experimental studies[62] on PnC slab resonators at GHz frequency range.

The PnC structure used to design the resonator is made by drilling a square array of cylindrical holes in an aluminum slab with similar parameters as discussed in the previous Section. As shown in the previous section, this PnC slab provides a large complete PnCBG with frequency extent of 140 kHz < f < 185 kHz allowing for confinement of mechanical vibrations in that range. The most basic PnC resonator presented in this section is made by removing one period of PnC holes from the PnC structure and thus creating a PnC cavity, as demonstrated in Figure 2.11. The cavity is surrounded by two periods of holes on each side in the direction perpendicular to the wave propagation direction (x-direction) on each side and is considered very large compared to the wavelength in the perpendicular direction (y-direction, Figure 2.2).

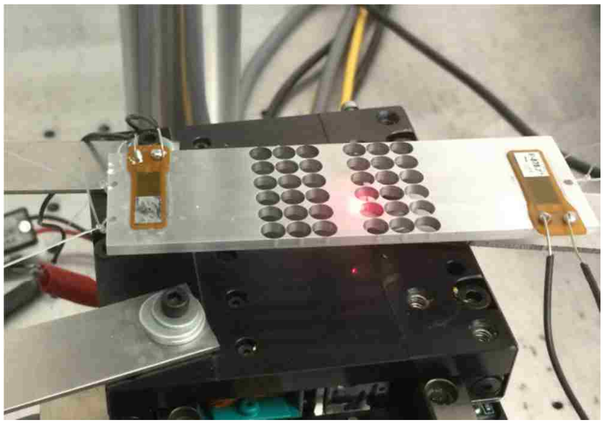

Figure 2.11 Al-Air Resonators with a=8mm and r/a=0.48 and t/a=0.5.

First, frequency domain analysis was performed to study the cavity devices. Different defect sizes were tested. Figure 2.12 shows W-1 cavity with the same parameters as PnC, shows two resonance frequencies at 156 and 170 kHz with a good separation from the limits of ABG, so a good confinement is expected.

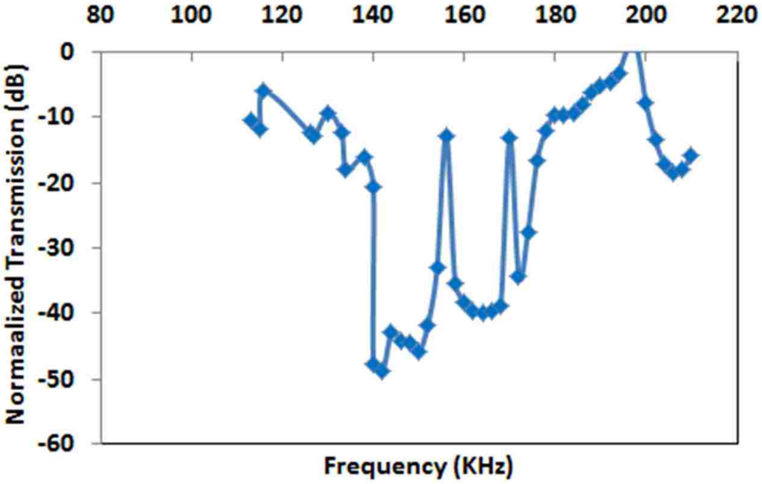

Figure 2.12 Experimental transmission results of a PnC formed from a cubic array of Al-air PnC with r/a = 0.48, t/a = 0.5. It displays a bandgap between 140 to 185 kHz.

The experimental result of measuring the transmission through the PC resonator to the transmission measured through the slab with the same parameters but without the PC holes (Al slab) is shown in Figure 2.13. As is shown in that figure the resonant mode excited within the complete ABG of the crystal can be seen. The resonance frequency of the first mode is approximately at 152 kHz while the resonance frequency of the second mode is at 170 kHz, which is very close to the upper limit of the absolute acoustic bandgap. Since the resonance frequency of the first mode has enough frequency separation from the edges of the absolute bandgap.

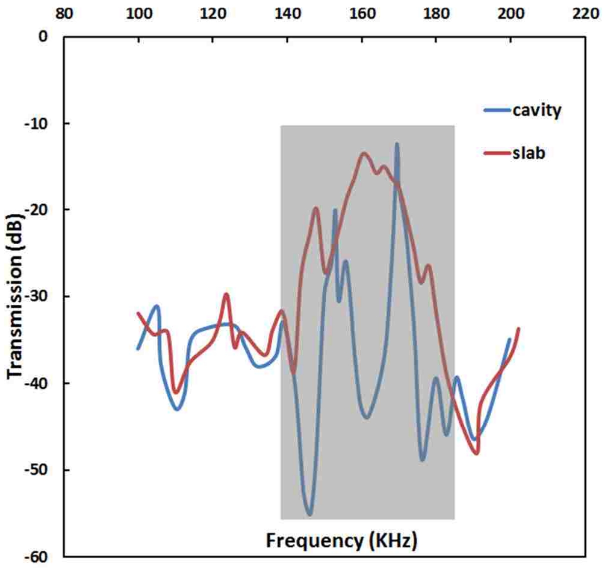

Figure 2.13 Experimental results of transmission through (Blue) PnC slab cavity structure (Red) Al matrix. The shaded region denotes the ABG.

One of the important factors in designing resonators is the Quality factor and for these PnC cavities it is 102 for the first mode and 178.4 for the second mode and they are not as high as the as high as the micromechanical resonators reported in the literature. A main reason of the low values of Q is the limited number of PC layers (only two periods) around the cavity. Mohammadi et al. have shown[63] that with adding one row the quality factor enhances by a factor of five. Besides testing the resonators in vacuum could help, increasing the quality factors.

2.4.4.3 Waveguide

Waveguiding is one of the most necessary applications of the PnC devices. By locally introducing defects and modifying the PnC structure (e.g., by changing position, size or geometry of the inclusions) one can create a waveguide. A waveguide forms by introducing line defects in the phononic crystal structure parallel to the wave propagation direction and elastic waves can be and guided along the line defect through the crystal. To establish the possibility of waveguiding in macro PnC structures, I designed and made a simple Single Mode waveguide by introducing a line defect in the square lattice of the PnC slab structures. Both Longitudinal and Flexural waves are excited using piezoelectric transducers. A similar set of transducers are placed on the other side of the PnC waveguide to sense the transmitted elastic waves. (Figure 2.14)

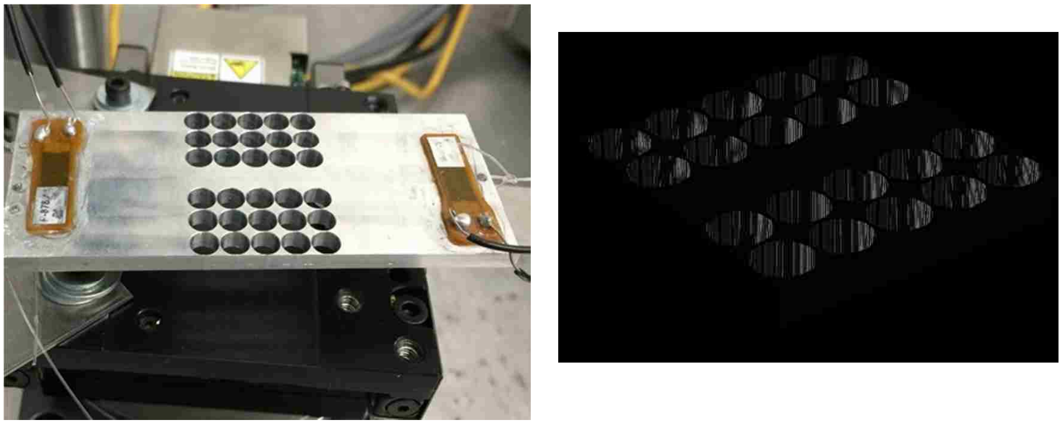

Figure 2.14 Suspended waveguide on the experimental platform with a=8 mm, r/a=0.48, t/a=0.75.

The lattice constant for this single mode waveguide is 8 mm and the r/a ratio is 0.48 and the t/a equal to 0.75. Figure 2.15 shows the band diagram and the inset proves the mode shape of the guided mode.

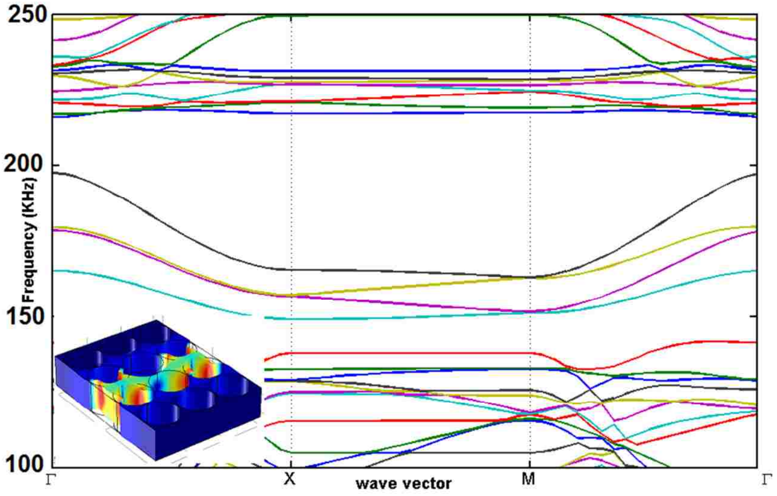

Figure 2.15 band diagram and guided mode shape, the parameters for the waveguide are as follow: a=8mm, r/a=0.48, t/a=0.75.

The transmission spectrum through the waveguide is shown in Figure 2.16. The expected PnC Band Gap region is shaded in this figure; it can be seen that the transmission drops at the edge of the expected BG and goes back up on the other edge of the predicted PnCBG as expected.

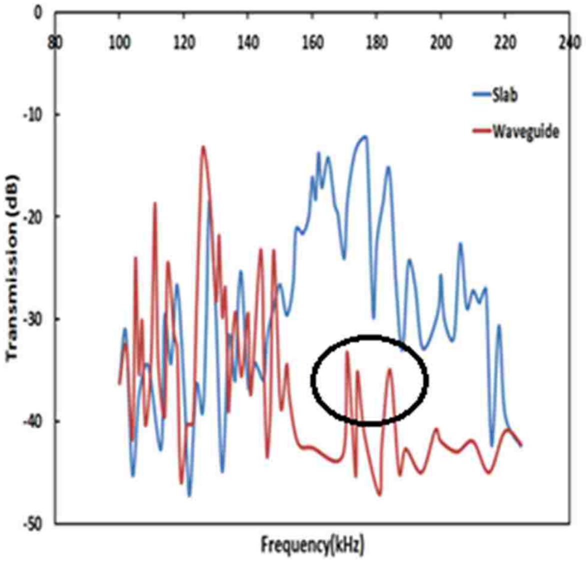

Figure 2.16 Experimental results for the waveguide, the guided modes are shown in the black circle

However, unlike the measured transmission through the perfect PnC structure, there are some frequency regions in the BG that show good transmission through waveguide structure. These regions correspond to the modes of the PnC waveguide. As can be seen from Figure 2.16, there is about 5 – 10 dB loss observed in the transmission of waveguide modes through the PnC slab waveguide structure.

2.4.4.4 90° Bend:

Wave bending in phononic crystals, based on band gap effects, has attracted recent and growing interest[21,64]. However, there is no study that has been done experimentally that shows the bending of waves in a plate with defects. In order to prove that an L-shaped guide formed was designed by introducing a line defect into the crystal. Since the propagation of the mechanical waves is forbidden in any direction at certain frequency range (BG frequency range), mechanical waves are confined to the guide, at these frequencies. Therefore the existence of a full band gap is necessary.[11]

Also Splitter is another useful waveguide device that divides the power in an input wave guide equally between two output waveguides, if the geometry is symmetric. This effect is achieved by creating a line defects in with in T/Y-shaped guide Like all other devices; the phononic band gap eliminates transmission for a range of frequency and reflected them back.

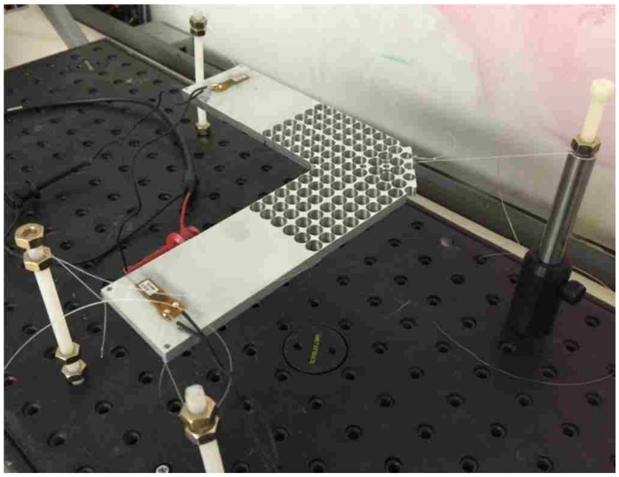

Figure 2.17 a)Suspended 90^{o} Bend structure with a=8mm, r/a=.48 and t/a=0.75 shwoing bending of acoustic waves in kHz range.

The aim of this part is to show experimentally that the guiding and the bending of acoustic waves can be attained in a tight space in highly confined waveguides constructed by introducing a line defect to a perfect two-dimensional phononic crystal. The greatest result is the experimental demonstration of wave transmission through a bent waveguide over a large frequency range, in accordance with our theoretical predictions.

The specific arrangements considered experimentally are shown in Figure 2.17. The Phononic crystal device is composed of a two-dimensional periodic array of an Al-Air. The square lattice constant for both 90 degree bend and splitter is 8 mm and the r/a ratio is 0.48 in 6 mm(t/a=0.75) Al plate. For this arrangement COMSOL Eigen Frequency modelling is used to theoretically study the behavior of the crystal. The band diagram for the straight waveguide is shown in figure 2.18a.

Experimental transmission spectrum is shown in Figure 2.18b. This graph for the very first time shows the experimental demonstration of propagation and bending of acoustic waves in a specific range of frequency.

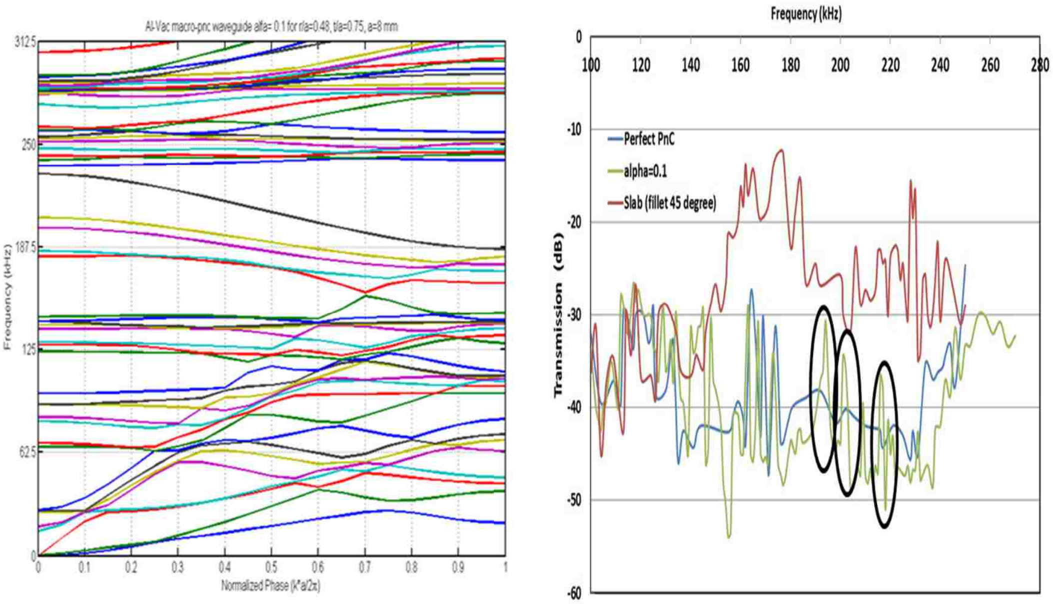

(a) (b)

Figure 2.18 a)Numerical and b)Experimenat results for 90° Bend and splitter for perfect crystal (with no defect) devices with a line defect removing one row in the crystal.

2.5 Conclusion

In this chapter, governing equations for analytical study are introduced as well as two main efficient FEM methods. Those methods are utilized for the 3D analysis of PnC structures of different arrangements and architectures. These include Eigen frequency and Frequency domain analysis. The Eigen frequency helps to extract bandstructure and mode shapes for any wave vector. Frequency domain analysis would provide a transmission analysis over a certain frequency range. Each of the tools has been used based on the simulation and analysis needs.

The structure is made of a 2D array of cylindrical void inclusions embedded in an aluminum slab with a finite thickness. Full 3D simulations using the COMSOL Multiphysics are performed on these PnC slabs to find the PnCBGs for various array lattices and geometries, and optimal structures are chosen.

An excellent platform for observing the unique properties of PnC structures is introduced. This platform can be utilized to study fundamental devices such as waveguides, resonators and etc. Great PnC characteristics can help to understand the fundamentals of such devices.

Five main pnC devices are designed, fabricated and tested and results are reported. The simulation results obtained using these methods show very good agreement with each other and also the experimental data.

It should also be noted that the resonator reported in this work, can be considerably developed and improved in several aspects. By adding a few rows to the resonators the Q of the resonant modes can be significantly improved.

PnC waveguides are designed, analyzed, and demonstrated by modifying line defects within the PnC structure, and also it is been shown the elastic waves can be guided or bent with low-loss characteristics in waveguide types structures such as splitters and 90^o bend.

3 EXTREMELY HIGH FREQUENCY ALN MICRO PNC DEVICES

In this chapter, my main efforts toward implementing Piezoelectric materials as the host material for PnC structures operating at high frequencies appropriate for wireless communication and sensing applications are reported. The periodicity in these PnC devices is obtained by etching a 2D array of cross-type inclusions in an Aluminum Nitride (AlN) slab. There are only a few studies show the existence of bandgap in AlN devices. The existence of bandgap in the PnC slab and high frequency mode in the resonator is demonstrated.

In Section 3.1, a background for micro PnCs and Saw devices is provide and such PnC structures for controlling SAWs are investigated and analyzed using COMSOL Multiphysics software. The PnC used to develop the micro mechanical resonator is made by embedding square array of cross-type holes in a thin AlN. This PnC is designed to yield large complete PnCBGs (PnCBGs in all propagation directions in the crystal and for all types of waves) at a very high frequency. A resonator is also designed by removing two rows of unit cells in the PnC, which allowed confinement of vibrational modes through the PnC structure.

In Section 3.2, PnC structures and devices such as resonators are made of an array of Cross-type inclusions etched into a suspended AlN slab are fabricated and experimentally tested. Details of fabrication process and their geometrical parameters are explained. Such large PnCBGs serve as appropriate platforms for AlN Micro Mechanical PnC devices to be designed and used for wireless communications and sensing applications.

3.1 PnC Saw Structures

During the last decade, the propagation of the elastic waves in periodic or random composite structure has gained much attention[8,65]. Phononic crystals (PnCs) are structures that mechanical properties vary periodically[66]. One of Their unique abilities is to exhibit a wide acoustic bandgap for certain ranges of frequencies. Bandgaps are ranges of frequencies that waves don't propagate through the structure[9]. Previous studies have shown the versatility and tunability of frequency band structures in PnCs by manipulating the geometry and introducing defects. This great capability allows for confinement, wave guiding and focusing of mechanical energy[60,67]. Because of their low loss and high quality characteristics these devices have applications in wireless communications, opto-mechanical coupling devices and modulators, etc.

Recently several numerical and experimental studies on 2D PnC slabs with finite thicknesses were performed and large acoustic bandgaps have been demonstrated in PnCs made of Si, SiO_2, SiN_x and SiC as the matrix and W and air as the inclusion[42,46,57,68]. Different types of lattices such as square, hexagonal with circular inclusions[69,70]. In addition, in order to achieve wider band gaps, recently some other designs were recently proposed and tested such as fractal, snowflake and IABG and hybrid[45,47,48,71].

Although some of those results demonstrated the existence of PnCBGs and also localized modes[72], theoretical and experimental studies show that confined modes in the defected structures energy leakage since 3-D structures might have propagating downward to the half space and also this loss may occur because of the folding[73].

The electrodes to sense and launch the waves are usually made of piezoelectric materials such as Aluminum Nitride (AlN) and Zinc Oxide. Piezoelectric materials are recently used as the host material[49,74] to reduce the insertion loss from the electrodes to the substrate and attain better confinement.

It has been shown that although PnCBGs can be obtained in PnC SAW structures and used for some applications, they are suitable for many applications such as realizing low loss resonators and waveguides due to the huge amount of loss of surface acoustic waves into bulk waves[72].

In this chapter, ultra-high frequency PnC slabs and micro cavity were designed, analysed and tested. The PnC used to develop the micro mechanical resonator is made by embedding square array of cross-type holes in a thin AlN. The existence of bandgap in the PnC slab and high frequency mode in the resonator is demonstrated.

The PC structure designed in this work is made by embedding a simple cubic array of cross type inclusions in a thin AlN matrix, as shown in the Figure 3. 1. This figure shows a unit cell of the PC structure in which d is the thickness of the PnC structure, a is the lattice constant, and w and l are the width and length of each cross hole respectively. For this PnC structure, the geometrical parameters are as a=3.4 µm, d=1.5 µm, w=800 nm and l=2.61 µm.

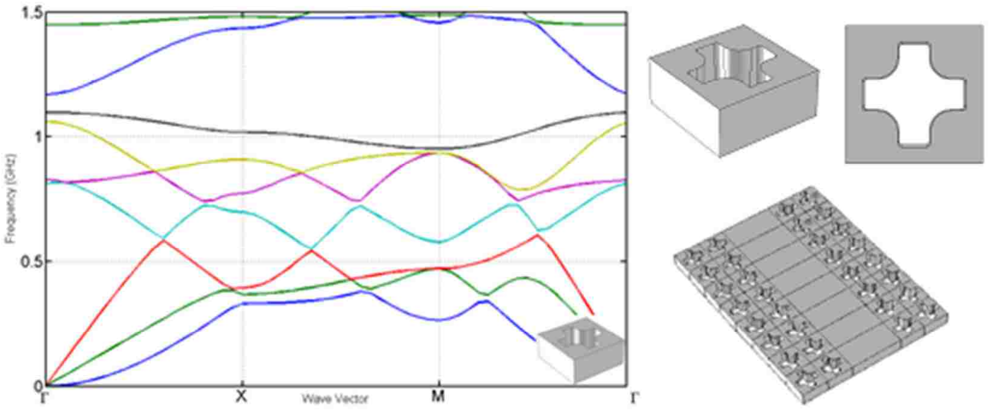

Figure 3.1 The band structure of a simple cubic lattice PnC of cross type holes in AlN slab with lattice constant, a=3.41 µm, width and length of each rectangular hole, w=800nm,=2.6 µm and slab thickness, d=1.5 µm. A unit cell of the structure is shown in the inset. (right) the unitcell and the designed cavity that is made in the PnC structure by removing two rows of holes from the PnC structure.

To find the bandgap frequency three dimensional COMSOL Finite Element Method (FEM) Multiphysics model was used for the design and the confirmation of the frequency band gap. Moreover, a PnC cavity was designed with the same geometrical parameters and by removing two periods of unit cells in the PnC array (W-2 cavity) and leaving three rows on each side of that line defect to support certain vibrational modes across the PnC.

The band structure of the first symmetric Brillouin zone of the PnC structure is extracted from the COMSOL Eigen-frequency analysis and is shown in Figure3. 1. The structure is simulated by applying the stress-free boundary condition in the z directions. It is clear that, this geometry provides an ABG with frequency range in

1095 MHz< f<1170 MHz which corresponds to 6.6% gap to midgap ratio, and allows to design other PnC devices to confine mechanical energy.

3.2 Fabrication and Experimental Procedure

3.2.1 Fabrication flow and processing of AlN PnCs

Similar to most MEMS devices, the fabrication process for a Phononic Crystals (PnC) consists of a combination of material deposition and material etching steps followed by a device release step. The process flow for creating a PnC is described below. The PnCs and the interdigitated transducers were fabricated in a 7-mask CMOS compatible process.

High-resistivity (>10k Ω-cm) silicon wafers are selected as the substrate material. A 600 nm-thick oxide deposition is followed by the deposition of a 2 μm undoped poly-Si release layer. Patterning and subsequent etching of the polysilicon layer are done to the level of deposited silicon dioxide layer. Next, a 3 μm PETEOS (Oxide) layer is deposited followed by Chemical-Mechanical Polishing (CMP) of this oxide layer to the level of the poly-Si layer (Fig. 3. 2). 200 nm PETEOS (Oxide) layer is deposited on top of the polished layer.

After patterning and etching of 600 nm of the oxide, a 1.2 μm chemical vapor deposited (CVD) to make the Tungsten (W) contact. W layer is laid on the etched region overlying the poly-Si. CMP is utilized to create a uniform surface and remove any excess material from the surface. Next, the bottom electrode layer (Ti/TiN/Al/Cu) is sputter-deposited and patterned.

Then, 1.5 um AlN is deposited on top. Etching of the AlN is done through a patterned photoresist layer above it. The PnC-based devices are formed through pattering the AlN layer. Metal Patterning of the metal contact is performed by first sputtering of 200/50 nm Al/Cu/TiN followed by etching this layer will serve as the top electrode for the transducers. (figure 2b). The width of each electrode depends on the targeted center frequency and the average sound velocity in the electrodes.

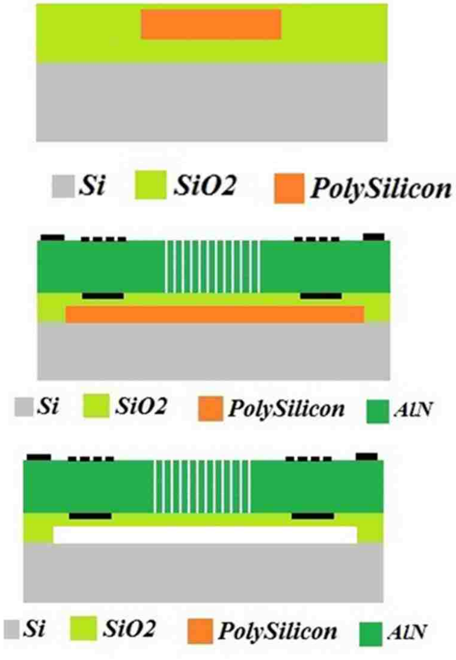

Figure 3.2 Poly Silicon layer was deposited on the oxide which was previously deposited on the silicon substrate. 100 nm deposition of bottom layer oxide is followed by deposition 1.5-µm-thick AlN layer. Then PnC devices are patterned. Subsequently Top electrodes with 100 nm thickness are sputtered. The entire device is released from the ploy silicon substrate by XeF2 isotropic dry-etch process.

Next, a 100 nm PETEOS oxide layer is deposited over the entire device. Anisotropic etching of Oxide is done to open the electrode pads and to expose the poly-Si layer by selective etching of Oxide to poly-Silicon. The poly-Si layer is released by Isotropic etching with XeF_2 (Figure.3.2). This results in a suspended air-bridge device configuration, thus reducing loss to substrate.

A large number of devices (~ 80) with the same PnC structure but with different electrode width were fabricated in order to characterize the entire frequency range from 950 MHZ to 1.25 GHz . For each set of electrodes, an identical device with no inclusion (AlN slab) was also fabricated with the same as the PnC structure.

The scanning electron microscope (SEM) image of the micro-fabricated presented in Figure3.3. Integrating the appropriate electrode size, acoustic waves are launched toward the PnC devices. The zoomed-in top view (Fig. 3.3 right) of the unit cell is also shown. The size of the device in the X-direction is 0.8 mm, which is way larger than the wavelength of the waves that are studied in this work.

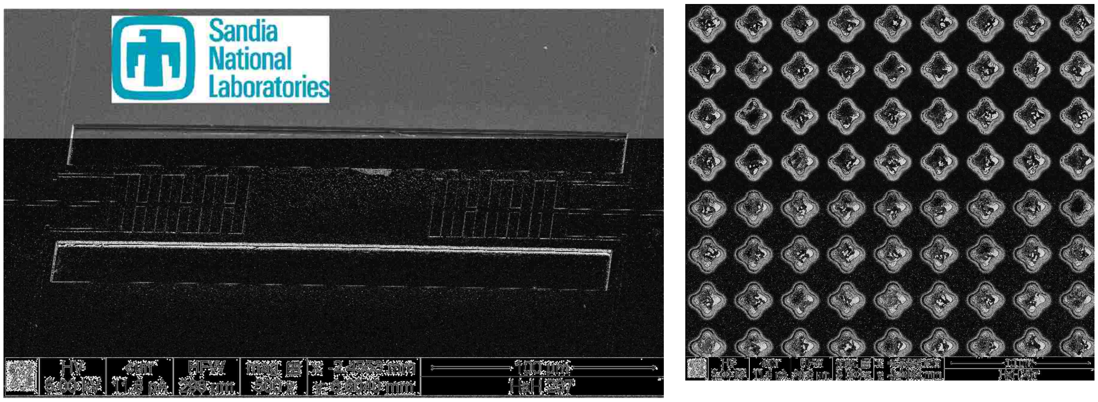

(a) (b)

Figure 3.3 (a) SEM of a fabricated AlN PnCs with drive and sense Al electrodes separated from each other by 15 layers of phononic crystals (b) zoomed SEM figure of PnCs(top view)

The PnC devices' response was measured using a direct 2 port transmission measurement via an Agilent network analyzer. All measured transmission is then normalized with reference devices, which consist of full AlN slab with no pattern (matrix). Then for the cavity the normalized transmission of the resonators to the matrix was calculated.

3.2.2 EXPERIMENTAL Setup and Procedure

As a result, the corresponding transmission spectrum along the gamma-X direction through PnC and the slab was measured separately. The normalized transmission response can be calculated by subtracting the transmission response of the reference devices (where no pattern exists (slab)), from the transmission response of the phononic crystal devices.

The transmission spectrum for both PnC and slab is presented here Fig.3.4. Low transmission coefficient in the frequency range 1110<f<1175 MHz can be observed. This is in excellent agreement with the theoretical predictions shown in Fig.3.1. One of the reasons for the bandgap being shallow (-20 dB) is the number of electrode pairs in the devices. Adding more electrodes will increase the fabrication cost and also make the entire device larger. This is one of the highest frequency bandgap achieved s by this date for PnC.

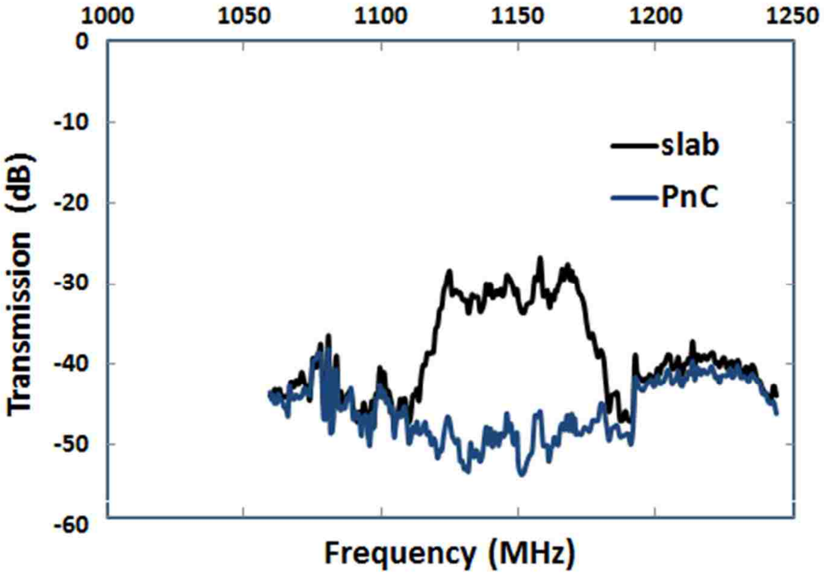

Figure 3.4 Transmission response of PnCs (purple) and reference (black).

In addition to the Perfect PnCs a micro resonator was also designed. Simulations also show that by removing two rows of PnCs and creating a w-2 cavity, there is a one transverse mode at 1122 MHz (out of plane) inside the bandgap. The total displacement field of the resonance mode is shown in figure 3.5

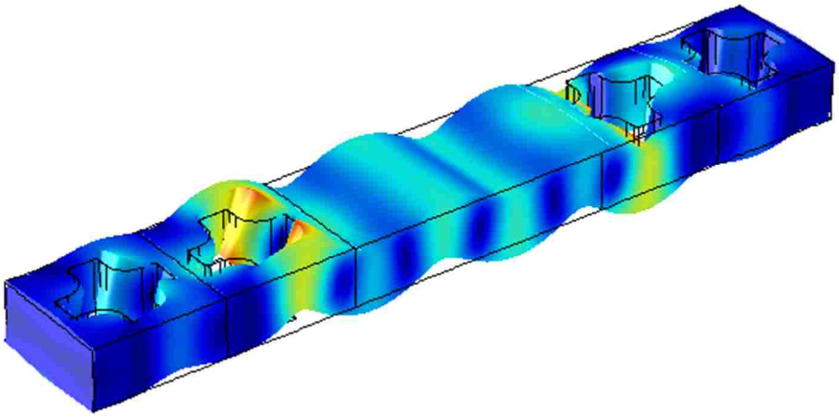

Figure 3.5 Mode profiles of the resonant frequency of the cavity structure.

This cavity was then fabricated and tested. The normalized transmission profile at frequency around the resonance frequencies of this resonator is shown in Figure. 3.6. As predicted, the peak associated with the flexural resonant mode of the cavity appears in the transmission spectrum of the waves passing through the PnC structure. This peak in the transmission profile is centered at 1117 MHz, is in a very good agreement with the predicted resonance frequency of 1122 MHz of the first studied mode found using FEM.

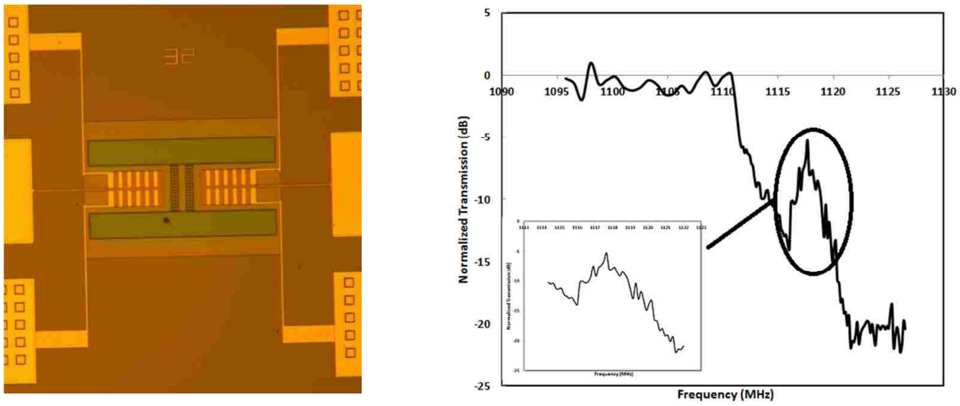

(a) (b)

Figure 3.6 (a) Optical Microscopic image of fabricated AlN resonators working at GHz Frequency (top view) (b) Experimental results of w-2 AlN cavity

Since this mode doesn’t have enough separation from the lower limit of ABG so a great confinement with high quality factor is not expected. The quality factor of this mode is around 400. As was previously discussed adding more periods will help to obtain better confinement.

3.3 CONCLUSION

The cross-type inclusion pattern Aluminum Nitride/air phononic crystals in a square lattice were designed and simulated in COMSOL to create an acoustic bandgaps and that devices have been fabricated and The transmission along the PnC structure, as presented in Fig 3.4, provides the experimental evidence for the possibility of achieving a large ABG in AlN PnC structure at extremely high frequency ranges.

This PnC design has also been utilized to show the existence of a confined mode in a micro resonator in AlN PnC. The cavity was achieved by removing two rows of unit cells in the PnC, which allowed vibrational modes to confine through the PnC structure with the quality factor of ~400. In the next chapter the possible ways to widen the bandgap ways will be discussed.

4 THE EFFECT OF STIFFNESS AND MASS ON COUPLED OSCILLATIONS IN A PHONONIC CRYSTAL

In this chapter, insight into phononic bandgap formation is presented using a first principles-type approach where phononic lattices are treated as coupled oscillators connected via massless tethers. The stiffness of the tethers and the mass of the oscillator are varied and their influences on the bandgap formation are deduced. This analysis is reinforced by conducting numerical simulations to examine the modes bounding the bandgap and highlighting the effect of the above parameters. The analysis presented here not only sheds light on the origins of gap formation, but also allows one to define design rules for wide phononic gaps and maximum gap-to-midgap ratios.

In section 4.1 the theory and FE Model of Inversed Acoustic PnCs (IAPNCs) is explained in detail. AlN/air PnCs are modelled using a structure from which simple inferences can be made to a system of coupled masses and springs. Changing the mass and stiffness of the system independently reveals physical insight into the behavior of the PnCs. The effect of tether length on band width of 3 different phononic Crystals is studied. It is observed that the bandgap become wider and narrow after a particular case for each one.

In section 4.2 for two different cases the band structure as well as the shape of each mode in the upper and lower edge of the bandgap is presented. The reasons for widening and narrowing the bandgap is explain based on the modal analyses. This analysis is followed by studying the effect of varying density on the mode movements and bandgap width. In particular, this arrangement lends itself to reinterpretation via a simplified coupled mass-spring system and allows a better understanding for PnC design optimization.

4.1 Inverse Acoustic PnCs:

Phononic crystals (PnCs) are periodic composite structures comprised of two or more linear-elastic materials of varying mechanical properties.[8,75] Structures of this type have the ability to inhibit the propagation of vibrational energy over certain ranges of frequencies, forming what are known as phononic bandgaps. Furthermore, this selective inhibition allows for the confinement, guiding, or focusing of mechanical waves if a defect is introduced into the structure.[9,63,67,76] An increasing number of applications for PnCs include highly selective yet physically small filters for telecommunications, lenses, couplers and other elements for acoustic imagers and opto-acoustic devices such as modulators and optical cooling. Generally, all such applications either require or benefit from the mode depleted nature of the phononic bandgap frequency range. As such, a primary point of focus for PnC design is to produce the widest phononic bandgap possible, given various structural and material constraints.

Experiments and numerical analyses for planar, micro-scale PnCs operating in the MHz range have been performed on structures comprised of Si, SiC, and SiO_2 as the host matrix material and air or tungsten as inclusion material.[41,42,71] More recently, there have been demonstrations that a hexagonal lattice of scattering inclusions provides a wider bandgap than other lattice types, such as a square lattice. However, the thickness needed to generate the wider bandgap is considerably more than that for the square lattice.[44] This complicates the excitement of mechanical waves in the PnC with surface-mounted interdigitated transducers (IDTs), which are commonly used for experimentation.[36] Thus, researchers are designing more exotic unit-cell topologies, such as crosses and snowflakes, in an effort to reach wider bandgaps and attain better confinement in defected structures.[45]

Aluminum nitride (AlN) has been commonly used as the piezoelectric material for IDTs[42,46], but is not as commonly for the matrix material of the PnC. However, due to its piezoelectric nature and compatibility with most IC manufacturing processes, AlN is a good candidate for the matrix material of PnCs.[47] The added benefit of this material is that a monolithic device can be manufactured that includes the PnC and the IDTs, thereby reducing insertion losses when compared to implementations that combine AlN resonators with other non-piezoelectric materials such as Si for the matrix material.

In particular, different classes of PnCs have been introduced recently by inverting the acoustic velocity distribution in the unit cell, where high acoustic velocity materials such as silicon or aluminum nitride are in the center of the unit cell and surrounded by a low acoustic velocity medium, *i.e.* cermet topology.[48] For a square-lattice PnC, the material in the center is connected to four thin tethers. With this type of structure it is possible to have high frequency bandgaps (*e.g.* 630 MHz for a lattice constant of 5μm) as compared to other types of structures with the same lattice constant.[49]

The geometries of the structures simulated and simulation view are shown in Figure 4.1. Central cylinders represent the majority of the mass of a system while the tethers, of length L_t, connect the cylinders together and add stiffness between the masses and dictate the deformation shape of the structure. Thus, to a good approximation the radius of the cylinders is directly related to the mass of the system, and the length of the tethers is related to the spring constant.

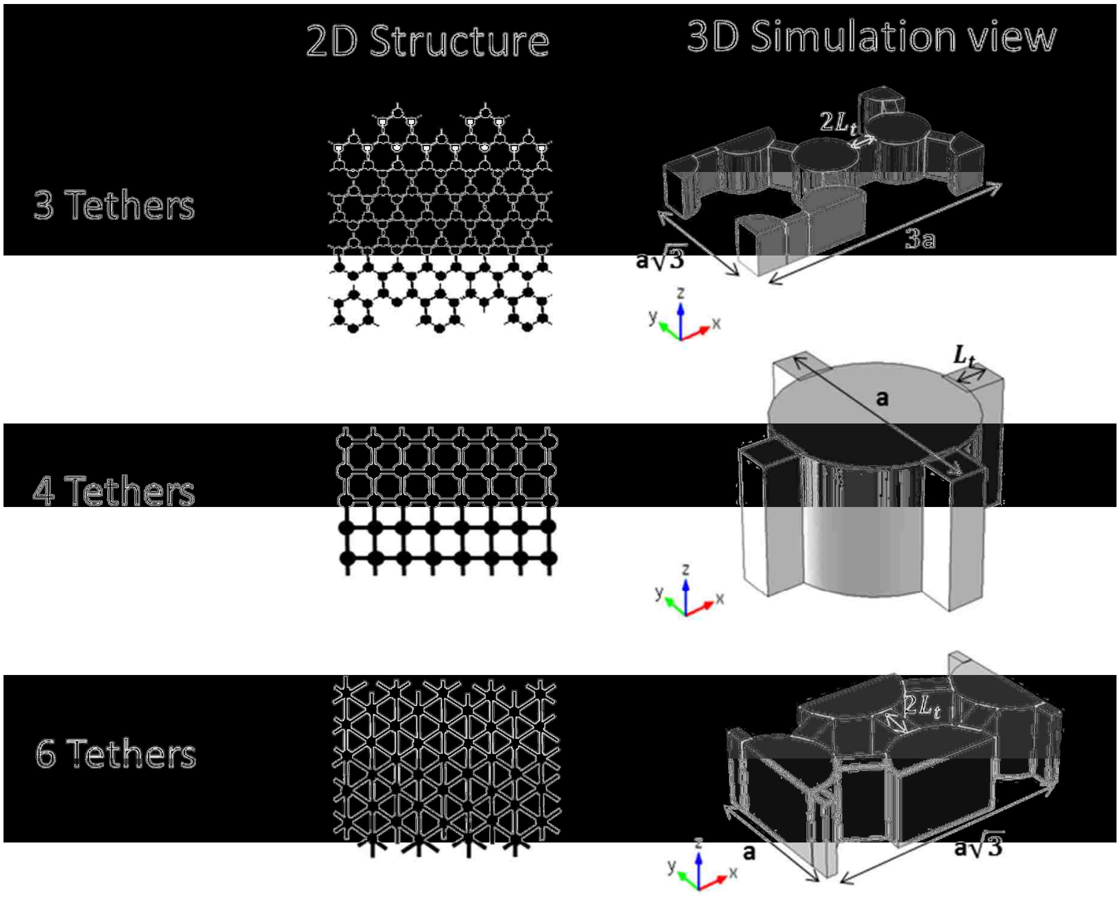

*F*igure 4.1 General structure of the PnCs considered in this work accompanied by the simulation view for the corresponding structures.

This assumption is used for the coupled oscillator analogy used to explain the physics bandgaps’ change in shape. The number of tethers per mass considered were 3, 4, and 6, since these are the first three configurations of a mass and tether system that yield a 2D network with tethers of identical length.

COMSOL Multiphysics was used for the simulations to determine the band diagrams and mode shapes of the excited structures while varying the length of the tethers and the mass of the system. Mass and stiffness are considered for all elements of the FEM. The Bloch periodic boundary condition was applied to the unit cells to generate the dispersion band diagrams. All possible modes of propagation were considered, *i.e.* in-plane, out-of-plane transverse, and longitudinal modes. Using the band diagrams, the primary bandgap widths can be determined, where the bandgap is defined as the frequency range for which no modes can propagate over the entire irreducible Brillouin zone.

The effect of varying the stiffness of the system was investigated by varying L_t from 100 nm to 2 μm while holding the mass of the system constant, *i.e.* the cylinder had a constant radius (1.8 μm). Each simulation for a discrete tether length results in a pair of frequency values for the upper and lower edge of that particular bandgap, thereby defining the bandgap width. The results of simulating multiple tether lengths and plotting the frequency pairs for each bandgap are shown in in Figure 4.2. Note that, the values for the upper and lower edge diverge and then merge again as the tether length is increased. Interestingly, the upper and lower edges of the bandgaps fall at different rates.

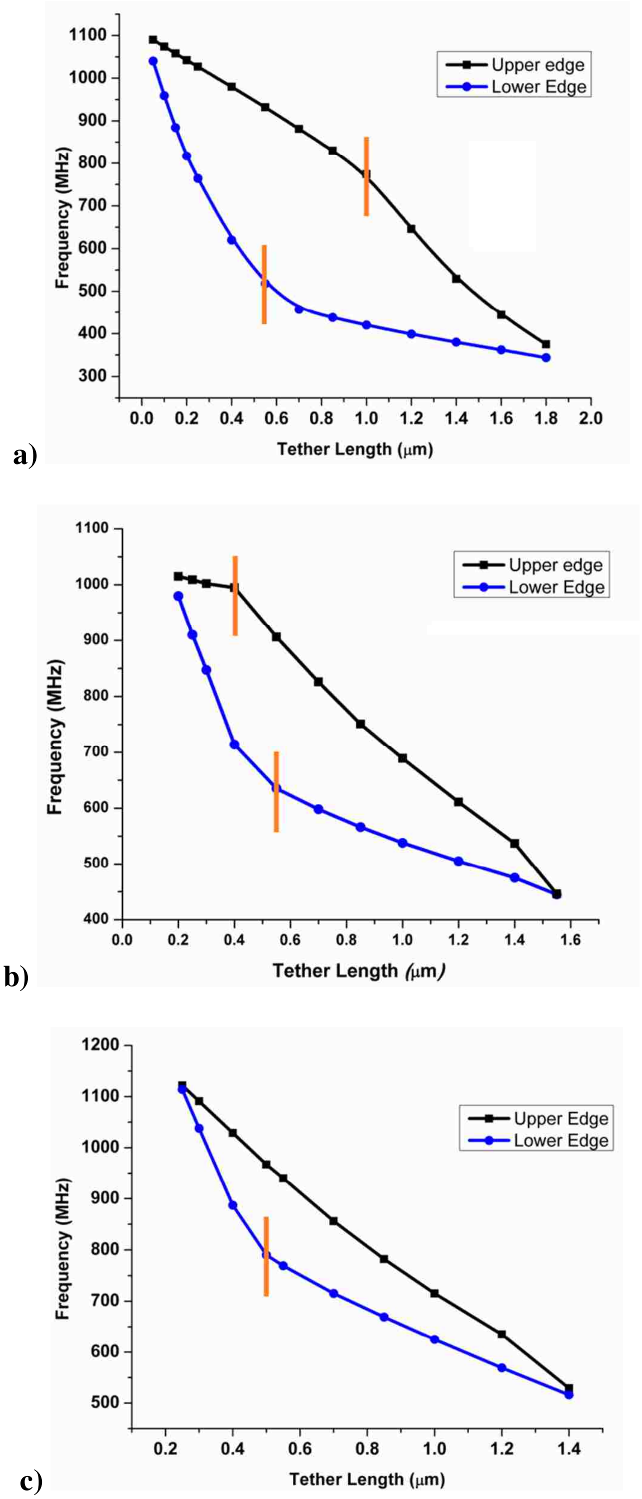

*F*igure 4.2 Bandgaps open and close as the length of the tether is increased with a constant mass for the **a.** 3, **b.** 4, and **c.** 6-tether cases. Vertical (orange) lines indicate the approximate position where kinks in the curves are found. These positions are where new modes overtake the old ones defining the bandgap edges.

4.2 Theory of Coupled mass-spring systems and Phononic Crystals bandgap width:

An examination of the mode shapes of the system at the upper edge and lower edges of the bandgaps reveals a vast change in the modal shape as a function of the k-space point, as shown Figure 4.3. One possible explanation for this modal change is that the active stiffness of the system around each bandgap is changing in type and value.

There are four different deformations possible for this 3D structure, given that a single tether has multiple stiffness values depending on the type of deformation it experiences.

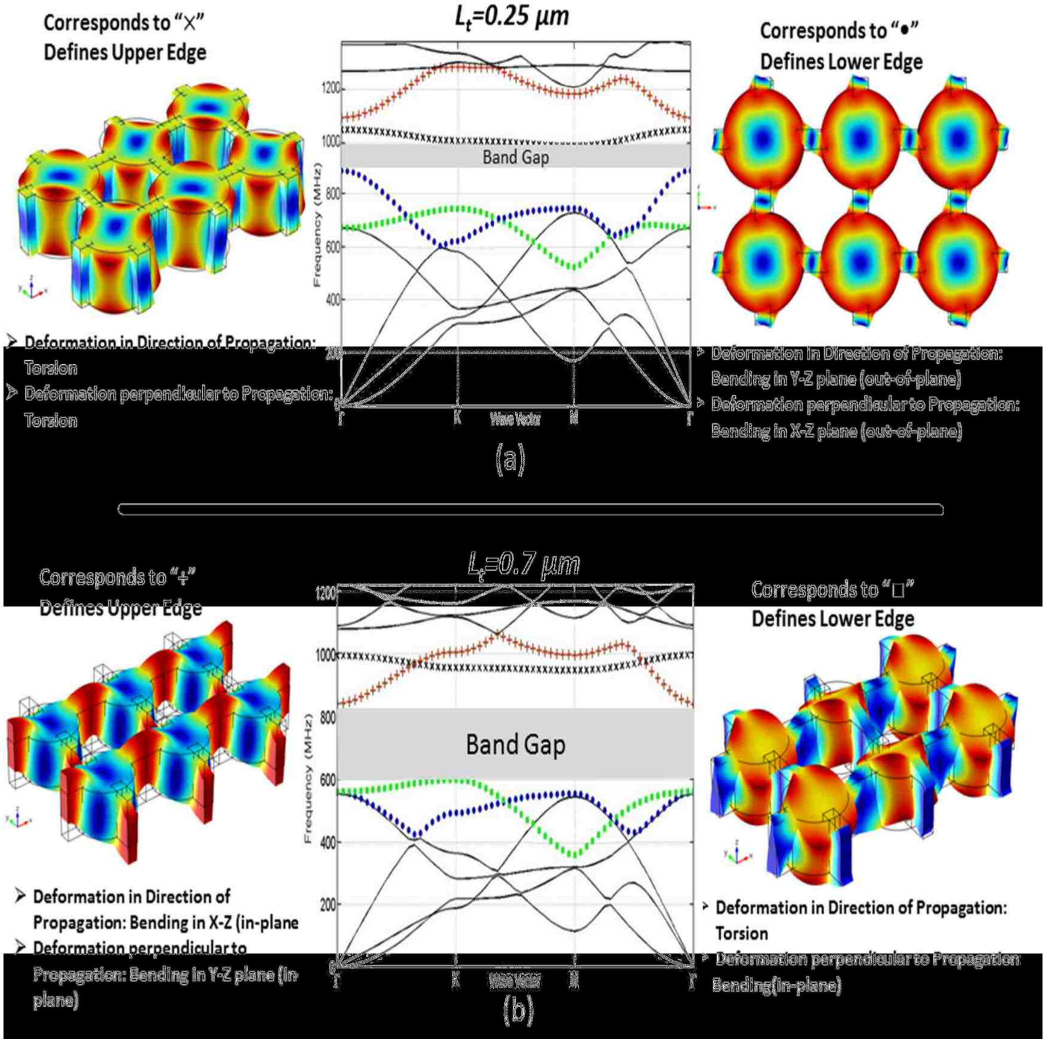

*F*igure 4.3 Effect of the tethers' lengths on upper edge and lower edge frequencies for a. L_t = 0.25 μm and b. L_t = 0.7 μm. Mode shapes are shown for the upper and lower edges of the bandgap. Deformations described are the primary modes of deformation. The red '+' symbols represent an in-plane bending mode, the black '×' symbols that represent a torsion mode, the green '■' symbols represent a mixed mode (in-plane bending and torsion), and the blue '•' symbols represent an out-of-plane bending mode.

Each tether can be deformed by: (1) extension – lengthening or compression along the axis of the tether L_t is defined on, (2) torsion – rotation about the axis of the tether

L_t is defined on, (3) in-plane bending – bending parallel to the axis of the tether L_t is defined on, or (4) out-of-plane bending – bending perpendicular to the axis of the tether L_t is defined on. The stiffnesses corresponding to each of these deformations are:

$$k_{extension} = \frac{EA}{L} \tag{4-1}$$

$$k_{torsion} = \frac{GJ}{L} \tag{4-2}$$

$$k_{bending\,\parallel} = \alpha \frac{EI_{\parallel}}{L^3} \tag{4-3}$$

$$k_{bending\,\perp} = \alpha \frac{EI_{\perp}}{L^3} \tag{4-4}$$

where E is the elastic modulus (410 GPa for AlN), A is the cross sectional area of the tether perpendicular to the axis L_t is defined on (700 nm in width and 2.5 μm height), L_t is the length of the tether, G is the shear modulus (125 GPa), J is the polar moment of inertia, α is a constant introduced by the boundary conditions for the tethers, $I_{//}$ is the second moment of inertia for the beam parallel to the axis of the tether L_t is defined on , and $I_{\perp}$ is the second moment of inertia for the beam perpendicular to the axis of the tether L_t is defined on. There is also a possibility that mixed types of deformation exist. The aggregate deformation of a single tether can be the result of multiple types of deformation experienced simultaneously. All tethers that are parallel to one another will be deformed in exactly the same manner due to the symmetry of the structures. As one tether deforms, the neighboring tethers with dissimilar alignments will deform in a complementary manner, sometimes resulting in mixed types of deformations depending on the positions of the tethers.

To examine how this proportionality change affects the modes around a particular bandgap, one needs to examine the rate at which the mode frequencies change as a function of tether length, *i.e.* $d\omega_n/dL_t$, while keeping the dimensions of the cylinder constant. The natural frequency, ω_n, of a system comprised of masses and springs is proportional to the square root of the ratio of the stiffness, k, to the mass, m, or:

$$\omega_n \propto \sqrt{\frac{k}{m}} \tag{4-5}$$

Examining Eqns. (1) for all cases, it is clear that increasing the length of the beam decreases the stiffness of the beam, thereby causing the natural frequency to decrease. However, the proportionality of the change with respect to L_t differs depending on the deformation type.

Since the oscillating cylinder mass is constant, the frequency changes only as a function of the length variation of the tethers. Referring to Eqns. (1) and (2), $d\omega_n/dL_t$ for extension and torsion is proportional to $L_t^{-1.5}$, whereas the bending deformations have $d\omega_n/dL_t$ proportional to $L_t^{-2.5}$. From these results, it is clear that ω_n is always decreasing for an increase in L_t, as observed in Figure 2. Furthermore, the bandgaps initially open and then close due to the frequencies of the modes of the lower and upper edges first diverging from and then converging to one another. Referring back to Figures 2a-c, one can identify that the curves demarcating the boundaries of the bandgap contain kinks. These kinks indicate the position where a new mode begins to define the extent of the bandgap. The new modes have frequency change rates ($d\omega_n/dL_t$) that are different as compared to the previous modes that defined the bandgap for lower L_t values. In the case of the upper edge modes, a mode with higher frequency change rate overtakes another, *e.g.* a bending mode. For the lower edge modes, a mode with lower frequency change rate overtakes another, *e.g.* torsion or extension.

Of the cases considered, the 4-tether case is the easiest to visualize the deformation shapes. Hence, the mode shapes for this case are discussed further here. Referring to the band structures of Figures 3a and b, there are four modes that are nearest to the bandgap. At the upper edge of the bandgap, the red '+' symbols represent a deformation mode that is primarily in-plane bending and the black '×' symbols represent a deformation mode that is primarily torsion. Initially, the torsional mode is the mode that defines the upper edge of the bandgap, but at a value of $L_t = 0.4$ μm, the in-plane bending mode becomes the mode that defines the bandgap. This happens because the torsional mode has a smaller $d\omega_n/dL_t$ compared to the in-plane bending mode, and as such after increasing L_t by some critical amount the torsional mode is overtaken by the in-plane bending mode (see Fig. 4. 3). For the lower edge of the bandgap, the green '■' symbols represent a deformation mode that is a mixed mode (in-plane bending and torsion) and the blue '•' symbols represent a deformation mode that is primarily out-of-plane bending. Initially, the out-of-plane is the mode that defines the lower edge of the bandgap, but at a value of $L_t = 0.55$ μm the mixed (in-plane bending and torsion) bending mode becomes the mode defining in the bandgap edge. This happens because the out-of-plane bending mode has a larger $d\omega_n/dL_t$ than the mixed mode, and as such after increasing L_t by some critical amount the mixed mode becomes the mode that defines lower edge of the bandgap (see Fig. 4.3).

Thus, the bandgap widens and constricts due to the differences in $d\omega_n/dL_t$ of the modes near the upper and lower edges of the bandgap. Initially, the bandgap is created because the upper edge mode is moving down slower than the lower edge mode as L_t increases. For the 4-tether case, the torsional mode is decreasing in frequency slower than the competing out-of-plane bending mode that occurs before both kinks in Figures 2b. However, after the kink points for the upper and lower edges, a faster descending mode (for the upper edge – in-plane bending) and slower descending mode (for the lower edge – mixed mode) come in play to define the bandgap. Beyond this critical value, the $d\omega_n/dL_t$ of the upper edge mode is greater than that of the lower edge mode, forcing the modes to converge onto one another. This results in closing of the bandgap.

A similar trend is seen for the cases with different numbers of tethers, as summarized in Figure 4.4. The peak in the gap-to-midgap ratio is found to be dependent on the mode of vibration induced. Bandgaps open and widen due to the increased rate ($d\omega_n/dL_t$) for lower edge modes with respect to the upper edge modes. Then after a critical value of L_t, the bandgaps begin to close due to inversion of rates between the upper and lower edge modes. Furthermore, it is found that the bandgap is wider for the cases with fewer tethers, all other parameters held equal. This is a consequence of reducing the number of pathways for wave propagation when fewer tethers are present.

Additionally, there is more material available for the transmission of waves when the filling fraction of air is lower (*e.g.*, for the case of $L_t = 0.7$ µm: the filling fraction for 3 tethers = 0.64, for 4 tethers = 0.51, and for 6 tethers = 0.4). Thus, having more tethers allows for greater transmission of mechanical waves.

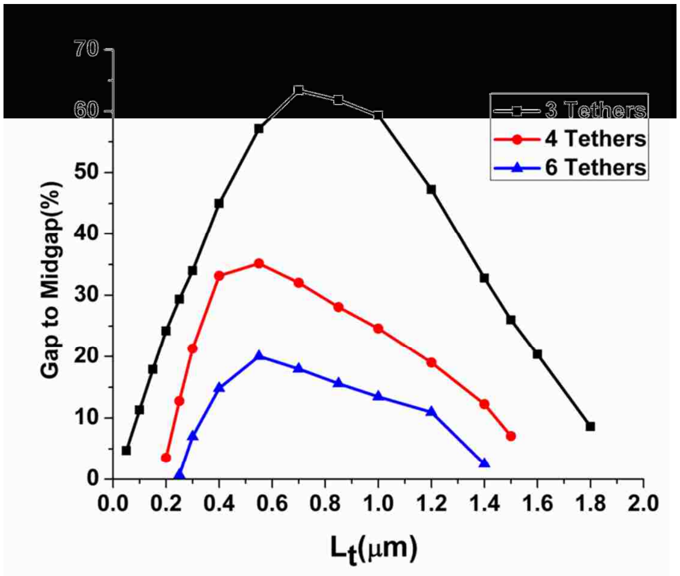

*F*igure 4.4 Effect of the tethers' lengths on the on the upper and lower edge mode frequencies for the 3, 4, and 6-tether cases.

A further reinforcement of our simplified mass-spring model comes from examining the effect of the mass on the mode frequency. According to the simple mass spring theory, the natural frequency of the system is given by $\omega_n \propto \sqrt{\frac{k}{m}}$, and thus is inversely proportional to the square root of the mass.

To validate the applicability of our model to the PnC system, the density of the constituent material is changed while all other system parameters, such as elastic and shear moduli as well as geometrical parameters (tether and mass dimensions, *etc*.), are kept constant. Figure 4.5 shows a logarithmic plot of the effect of changing density on the modal frequencies. It is evident that the slopes of both the upper and lower edges of the bandgap are -0.5, thus reinforcing the simplified model that we adopted here.

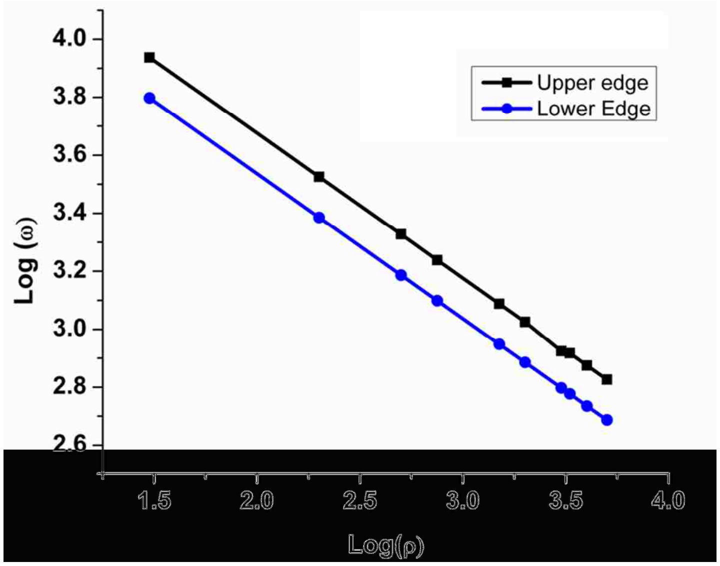

*F*igure 4.5 Upper and lower edge frequencies versus density of the PnC. The density of the material is changed while holding the tether lengths fixed. The frequencies of the upper and lower edges of the bandgaps change with $\sqrt{m}$ ($\sqrt{\rho}$).

4.3 Conclusion:

In summary, AlN/air PnCs were modelled as a system of coupled masses and springs using finite element model simulations. In-plane and out-of-plane transverse as well as longitudinal propagation modes were considered. Structures with 3, 4, and 6 tethers per mass in each unit cell were simulated to study the effects of changing mass and tether length on bandgap size and gap-to-midgap ratios. As the tether length is varied, the gap-to-midgap ratio was found to reach a maximum between two regimes displaying different mode characteristics around the same bandgap. Drawing from a simple system of connected masses, a metric, the frequency change as a function of tether length ($d\omega_n/dL_t$), was introduced to help identify the regime changes and thus the optimum bandgap width and gap-to-mid-gap ratio. While the bandgap defining mode characteristics and other specifics vary as the number of tethers per mass changes, the metric and method of estimation for the optimum bandgap width were shown to be consistent over the various geometries.

5 MODE SHAPE INVESTIGATION IN PHONONIC CRYSTALS

Photonic and phononic crystals belong to the group of metamaterials with designed properties not known in nature and they demonstrate unique properties such as sound focusing, wave confinement or wave guiding. In a phononic crystal (PnC), the periodicity of the host medium is used to manipulate mechanical vibration and mechanical properties. The guiding and confining acoustic waves can be obtained by introducing point or linear defects into the regular structure; these localized modes show resonant characteristics. This feature can be used for sensing purposes in sensors and filters[77] .

These modes can be designed to create well separated transmitting modes in the band gap (BG) or stop band outside the BGs. They demonstrate transmission peaks in the transmission spectrum of PnCs. The defect properties and geometry has a huge effect on these peaks. Most researches that deal with sensor, filters and telecommunications applications prove the sensitivity of the peak frequency on impedance mismatch between inclusions and host materials, defect size and speed of sound, c, in the defect material[78].

Phononic sensors will have a large impact in filters and sensors industry; they can also be used in analysis of complex systems. This especially applies to biosensors or medical sensors as well as chemical sensors for microreactors. These sensors utilize an approach to characterize complex molecules like proteins alternative to advanced spectroscopic measurement units. The ability of PnC sensors to determine volumetric properties of the different components onto a solid surface can be expected to become the feature in the near future. It is worth to note that, due to the lack of existence of any electronic component at the place of measurement the sensor has some significant advantages under tough sand severe environmental conditions as well.

In the future, higher frequency devices with reducing the device size or the motional mass may be achieved by using planar phononic crystals to form the mechanical resonator or splitters. Gradually shrinking micro/nanostructure device has so many applications in our day to day uses like the cell phones, telecommunication etc. It is very imperative to monitor the change of characteristics of the devices from the vibration or displacement. Phononic crystals also give the excellent opportunities of fabricating an integrated, chip-scale platform for routing and coupling optical and mechanical energy[74] if they are combined with Photonic Crystals (PhCs).

In this chapter, we consider a two-dimensional periodic square array of the air holes in a finite aluminum medium. The defect introduced to the crystals are acting as local acoustic resonances/guiding with the substrate and lead to the possibility of finding a low-frequency confined acoustic waves or guided modes. The numerical and experimental results presented here are related to the case of Aluminum-air devices, but the conclusions remain valid for other materials and compositions as well.

5.1 Experimental Setup:

A structure with N degrees of freedom will have N corresponding mode shapes. Each mode shape is an independent and normalized displacement pattern which may be amplified and superimposed to create a resultant displacement pattern. Studying the mode shapes will help to shed light on the origin of BG formation and as the results BG optimization. It would be beneficial to plot the mode shapes of the modes that limit the PnCBG in the band structure and in the ΓX direction. For instance, the mode shapes of the two bands that limit the PnCBG in this direction, which is the direction of measured transmission.

In this work, two different PnC devices i.e. a waveguide and a resonator were designed and manufactured. Modal analysis has become a frequently used method for studying the dynamic behaviour of mechanical structures. The mode shapes for those devices are calculated using the COMSOL finite element Software. The mode shapes were then studied using Laser Doppler Vibrometer. However, extracting the actual mode shape is not so easy because of to their small spot size and frequency of the PnCs. In this study, we used Laser Doppler Vibrometer (LDV) to observe the actual mode shape of the w-1 cavity and waveguide.

Polytec's single point LDV (OFV-534) head was mounted on a system of precision linear stages on the vibration isolation table. This LDV uses 1mW red laser (633 nm) to determine the position of a surface by heterodyne interferometry. LDV makes use of heterodyne interferometry to detect both velocity and displacement of a moving object. As can be seen in Fig 5.1 , the incident beam which is the reference signal and is generated by the LDV is compared with the signal that is the scattered (reflected back) light by vibrating (moving) object. The displacement of the PnCs is then determined by comparing the phase shift of the two light signals[79]. The output from the LDV is a voltage that is proportional to the target displacement along the direction of the laser beam, in this case since laser is perpendicular to the sample, out of plane displacement.

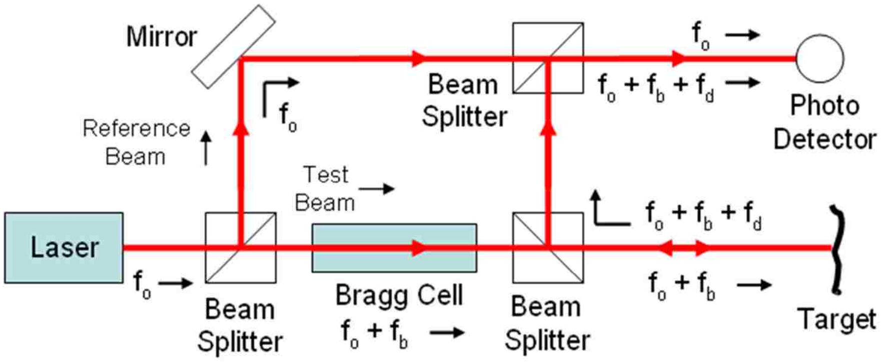

*F*igure 5.1 Schematic of laser Doppler vibrometer and its basic component

Laser Doppler Vibrometry has also become a standard method for studying real-time in- and out-of-plane surface mechanical vibration components of macro-sized objects[80]. Fig 5.2 shows the LDV that was used to map out all the points to visualize the mode shapes for PnC devices and out-of-plane displacement of PnCs. The whole setup is installed on an optical floating bench which helps to minimize the noise from the surrounding.

An X-Y stage with fixture is used to place the samples on the top of it and it is connected to a controller to help mapping out the whole surface. The principle of Laser Doppler Vibrometry (LDV) is the measurement of the velocity obtained by the detection of a Doppler shift in the frequency of coherent light scattered by the moving target. With this process light from a laser has to be projected onto a vibrating target, the backscattered light undergoes a Doppler frequency shift proportional to the target velocity and it is then coherently detected. The interferometric signal is usually processed by extracting the Doppler beat frequency through a frequency demodulator, so as to obtain an output signal proportional to the instantaneous target velocity.

*F*igure 5.2 Laser Doppler Vibrometer setup. It is fed by laser source from the top and the controller which is connected to X-Y stage presented

5.2 Results and discussion:

In this structure, Al was used as host material with air inclusions and the spacing between the closest holes (a) is equal to 5 mm, the radius of holes (r) is 2.4 mm($r/a = 0.48$), and the thickness of the slab (d) is 2.5 mm. The FEM result displays a complete frequency band gap centered about 260 kHz and ranging from ~220 kHz to ~300 kHz, which corresponds to a gap-to-midgap ratio of ~30 %.

This PnCBG allows for confinement of mechanical vibrations in that range. The most basic PnC resonator is made by removing one period of PnC holes from the PnC structure and thus creating a PnC cavity. The cavity is surrounded by three periods of holes on each side in the perpendicular to the wave propagation direction on each side. Also the waveguide with exact same dimensions was made by removing one row of holes and creating a line defect parallel to the wave propagation direction, so elastic waves can be and guided along the line defect through the crystal. Fig 5.3 shows the schematic of waveguide and resonator. The studied area is shaded with gray.

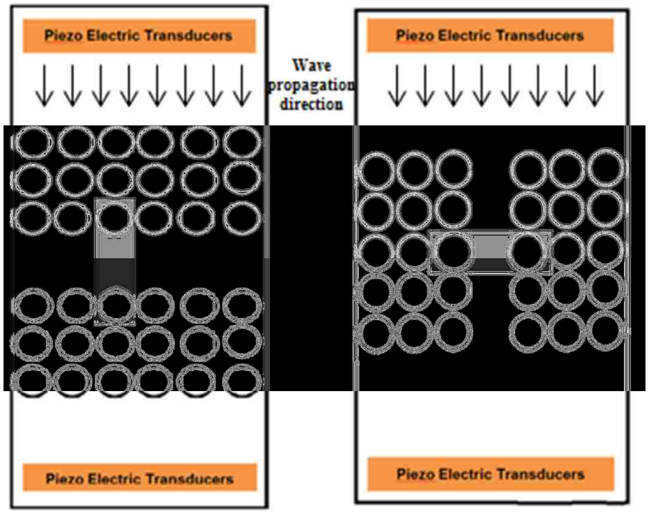

*F*igure 5.3 Schematic of the pnc devices, cavity (left) and waveguide (right)

In order to actuate the PnCs at desired frequency range, PZT are used to. Signal generation provided by a frequency generator, which provides a nominal 10 Vpp sine wave at desired frequencies. The phononic crystal is constructed from an aluminum block, with an inclusion pattern drilled through the plate. Isolation is obtained by fixing the crystal in middle of the air making a suspended bridge to avoid losses to the substrate and attain a better signal. This achieved by tying the crystal to a couple of semi-rigid pillars affixed to the test bed.

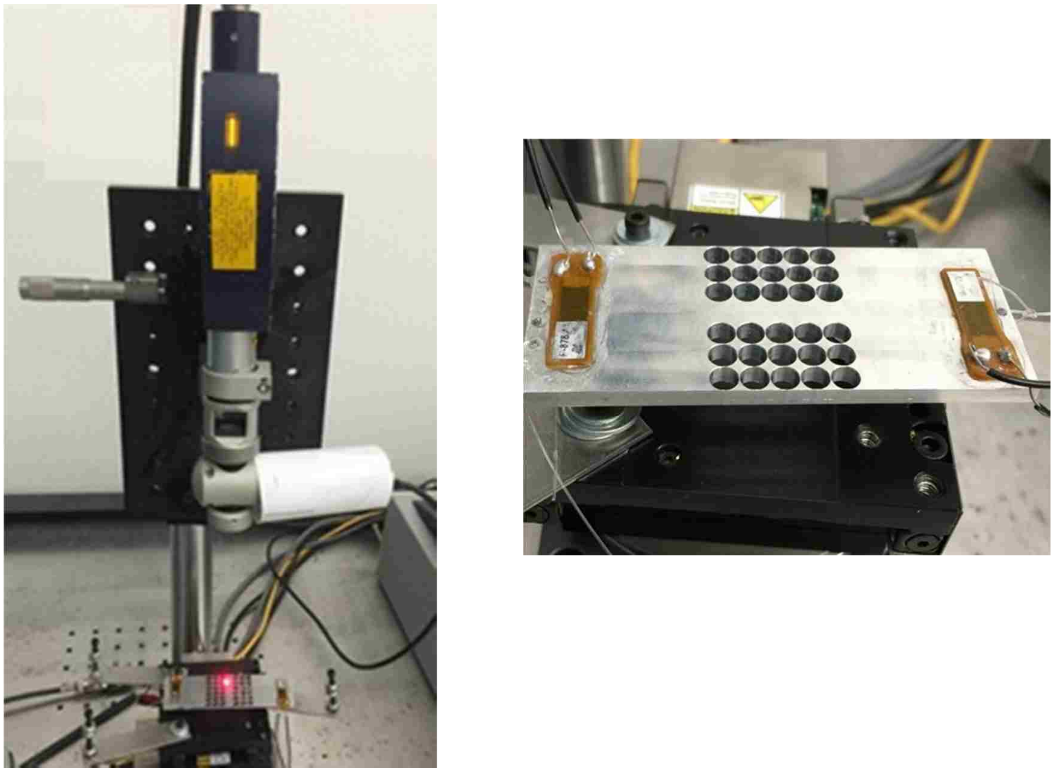

*F*igure 5.4 the suspended PnC sample on the stage

Based on the FEA the cavity and waveguide should show an out of plane modes around 260 kHz. For the waveguide there are more than one guiding mode exist, however in this study one of the cleaner out of plane modes is chosen. The actual mode shapes are shown in Fig 5.5 as well as FEA mode shape for the corresponding frequency. They look a little bit different from the simulated ones shown in Fig 5.5. proving the necessity to experimentally characterize and validate modelled data however the frequencies and shapes confirm the basic simulation model that has been used. The Fig. 5.5a shows that, in that case, the z component of the displacement field is localized to the vicinity of the defect area. The experimental data are then smoothened with MATLAB’s curve fitting tool and it is shown in Fig 5.5c. And In addition, locally large amplitude is found around the cavity’s defect area. It is worth to note that, this type of PnC devices are practically useful for control applications, and switched to different acoustic resonators.

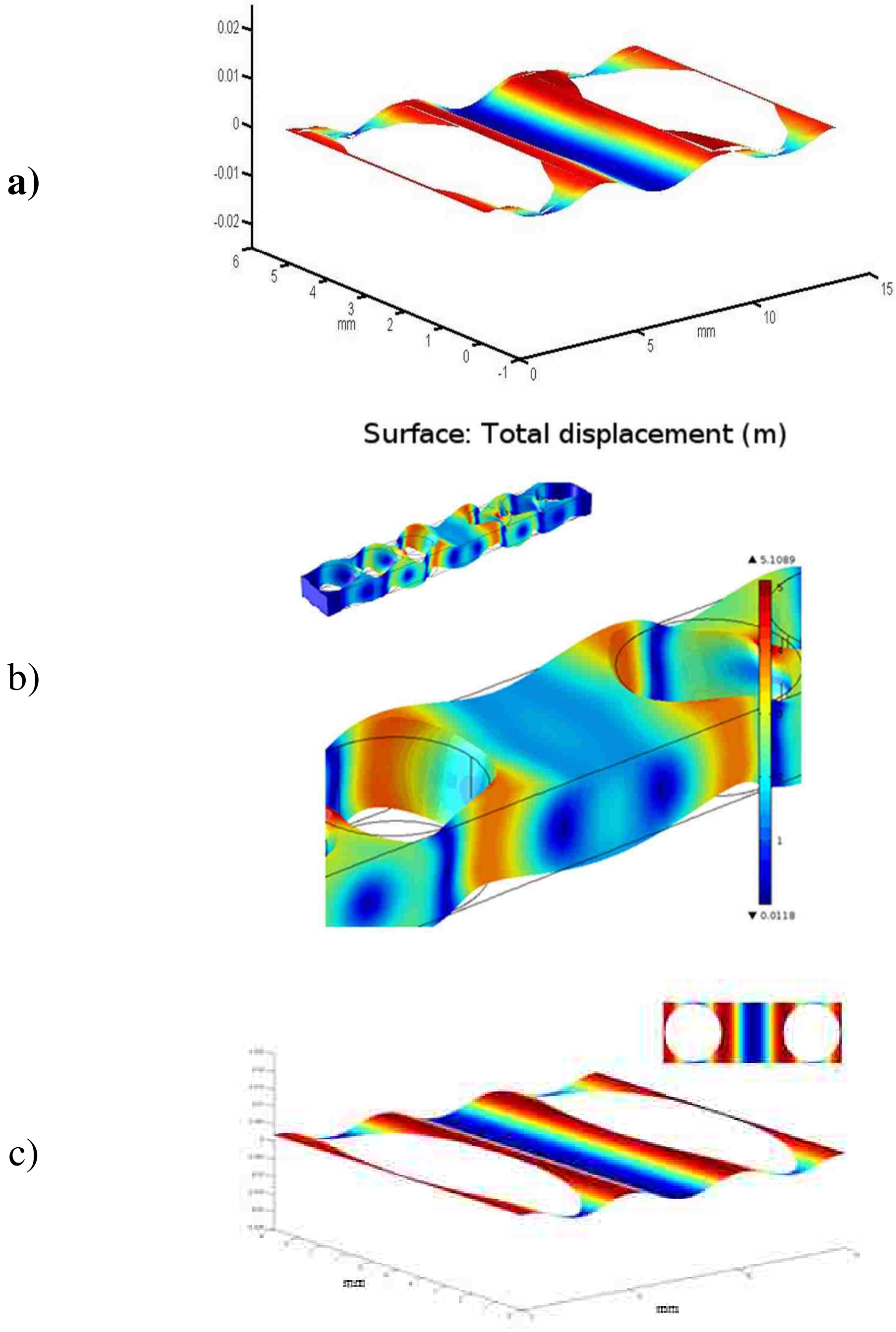

*F*igure 5.5 a) The experimental results using LDV b) numerical results using COMSOL c) smoothened experimental results

More over the experimental and numerical results for the waveguide is shown in Fig5.6. Experimental results prove that the elastic waves can be guided or bent with low-loss characteristics in waveguide types structures. The aim of this experiment was to show experimentally that the guiding of acoustic waves can be attained in a tight space in highly confined waveguides constructed by introducing a line defect to a perfect two-dimensional phononic crystal. The experimental results (figure 5.6b) show the evidence of waveguiding in PnC device. The experimental mode shape is very similar to what has been predicted with FEM.

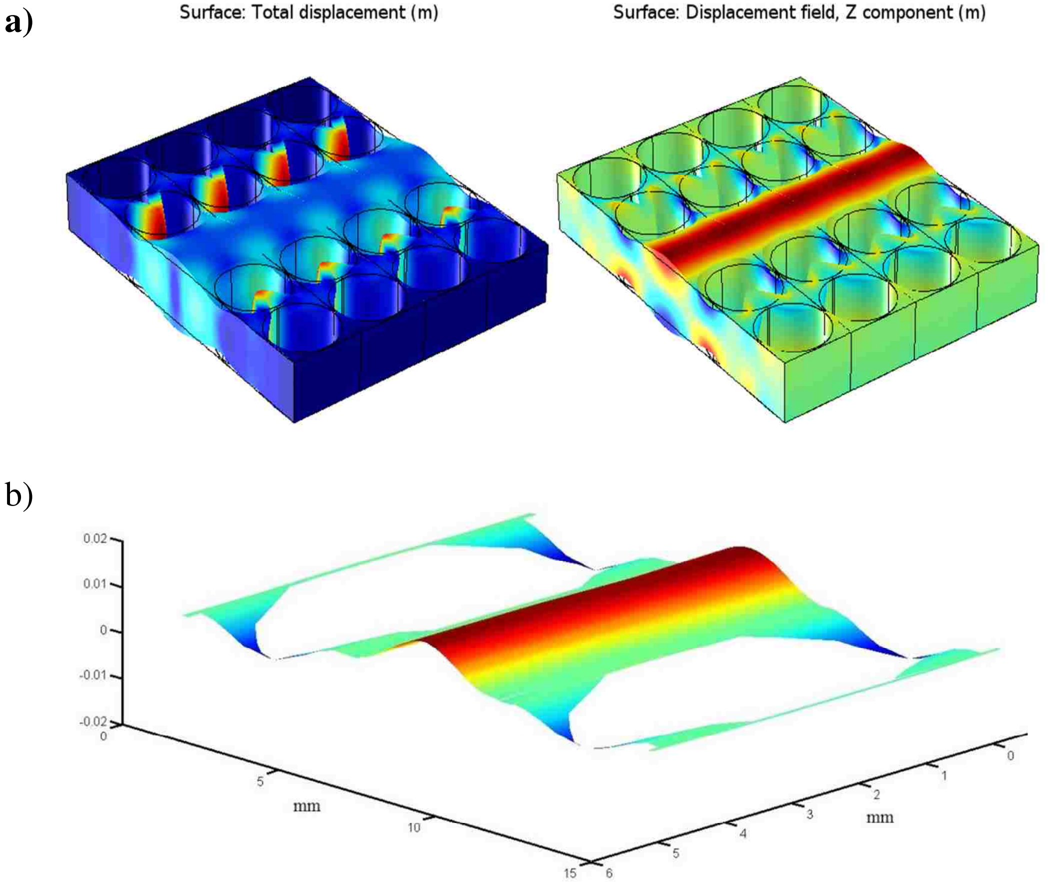

*F*igure 5.6. a) Numerical results using COMSOL, the left picture is total displacement and right picture is z component of displacement b) experimental results using LDV

It is worth to note that the mode is a mixed mode of out of plane bending with an in-plane bending mode.

5.3 Conclusion:

In summary, the study of the locally acoustic resonances and guiding modes with periodic square array of cylindrical holes (inclusions) in a finite aluminum substrate is presented for a w-1 cavity and waveguide. COMSOL Multiphysics was used to simulate the PnCs. The band structures of both devices demonstrate the presence of confined and guiding modes. Precisely, the presence of defect introduces new surface propagating modes.

Laser Doppler Vibrometer was used to study the mode shapes of PnC devices. The out of plane confined and guiding modes are studied and the experimental results are in a very well agreement with the simulation.

6 CONCLUSION AND FUTURE WORK

In this work macro-mechanical and micro-mechanical structures based on periodic arrays of inclusions are studied. It is shown that similar to Photonic Crystals that lead to a bandgap, a phononic (or acoustic) band gap (PnCBG) can be obtained in an integrated planar platform. The structures can be fabricated using standard macro/micro-fabrication processes based on either machining the part for macro size PnCs or utilizing lithography or etching for micro PnCs. It is demonstrated that this platform can be used to realize fundamental devices such as waveguides, resonators and splitters with outstanding characteristics and can improve key characteristics of such devices. A list of the main contributions made during the course of this work is given in the next section.

6.1 Contributions:

- Two different simulation techniques are introduced and developed and utilized for the 3D analysis of PnC devices. These include the Frequency Domain and Eigen Frequency analyses. The FE tools are developed by slightly modifying a commercial tool (i.e., COMSOL 4.2). Each of the tools has their own advantages and disadvantages and they have been used based on the simulation and analysis needs. The simulation results obtained are in a very good agreement with each other in several test cases and show very good agreement with the experimental data.

- Macro PnC SAW structures made of void holes in aluminum slabs have been analyzed, fabricated, and tested. An efficient and low loss platform for utilizing the unique properties of macro PnC structures is introduced. The structure is made of a 2D array of cylindrical void inclusions drilled in a solid slab with a finite thickness. Several devices such as waveguide, cavity and splitters have been analyzed and successfully tested. The results obtained were then discussed and suggestions to improve the performance of those devices were provided.

- Micro PnC made of AlN-air and a w-2 resonator were also simulated, fabricated and tested. The structures are designed to be compatible with planar micro/nano-fabrication technology, however, the studies suggest that although PnCBGs can be obtained at extremely high frequencies in PnC SAW structures, they mainly suffer from the loss of SAWs to the substrate and cannot be used to efficiently confine and control the propagation of SAWs. By developing and utilizing advanced fabrication processes and characterization methods, large bandgaps could be achieved in PnCs of different inclusions in piezoelectric slabs such as AlN.

- The arrangement and geometry of the inclusions in the array and the geometrical parameters of the structures are properly designed so that the structures support complete PnCBGs. Full 3D simulations using the developed tools are conducted on these PnC slabs to analyze the PnCBGs for various array configurations and geometries, and optimal structures are chosen. Excellent agreement between the experimental and the theoretical predictions is observed. More than 30 dB attenuation is achieved in the transmission of elastic waves within the PnCBG through only a few layers of the PnC structure; confirming the effectiveness of the PnCBG in stopping the propagation of elastic waves. This was (to our knowledge), the first experimental demonstration of PnCBGs in PnC slabs at such high frequencies.

- One of the first PnC resonators at frequency ranges appropriate for communications and sensing applications are designed, fabricated, and demonstrated. These resonators are made by surrounding a small region of AlN slab (i.e. a cavity) with the developed PnC structures. It is shown that very good confinement can be achieved, and high-Q resonant modes are supported within the PnCBG of PnC structures.

- Also one of the most important studies was investigation of band gap origin. In order to do that the mode shapes for the bandgap edge are studied. Coupled oscillation theory was utilized to investigate the mode rates as well as bandgap opening and closing. Besides for the very first time the experimental mode shape was observed using LDV. A w-1 cavity and a waveguide were fabricated and mode shape was verified with FE results. Very well agreement was achieved between experimental and numerical results.

6.2 Suggested Future Directions:

1- Analysis and development of the wave propagation loss in PnC structures and study the quality factor in resonators with different number of layers surrounding the defect and considering other sources of loss such as material loss.

2- Design and fabrication of high-efficiency micro/nanofabricated PnCs with different types of structures (inclusions and lattices) that can be beneficial as it may lead to achieve large PnCBGs with lower fabrication steps. Also use of different types of materials as the host material such as piezoelectric materials can lead to higher quality factors and more efficient devices. As an example using AlN layer as the piezoelectric materials was used in this work and it was advantageous compared to the relatively low quality sputtered zinc oxide (ZnO) reported in the literatures. Furthermore, using stiffer materials such as platinum and molybdenum can lead to devices with better characteristics but it might be costly and hard to fabricate.

3- An accurate frequency control is required in many applications and operating frequency of the devices should not vary drastically with environmental effects such as temperature, dust and etc. these sensors can be used in gaseous environments, liquid environments, therefore designing multilayered structures may lead to overcome that obstacle. Also they may be of great interest to design them in such a way that they sense the targeted species in a liquid environment.

4- As demonstrated in this work scaling and reconfiguring these structures can make highly efficient devices for telecommunication industry and other applications in the range of a few MHz up to GHz. Moreover, extending the ranges of frequencies towards higher regime (eg. THz), as the technology advances, can lead to controlling of thermal phonons which would be beneficial for energy management.

5- As was noted, these devices could be used in fluidic environment. In order to minimize the loss in those over damped environments the appropriate mode should be used. Mode shape analysis and optimization is beneficial to reduce the amount of attenuation in liquid

Periodic structures might have some applications that are not revealed yet but in the near future there might be even more applications such as negative refraction or efficient lensing. These were only a few of the applications of the PnC and PnCBG structures, and these devices can find their niche uses in different areas of micro/nano-mechanical systems.

7 REFERENCE:

1. Fang, N. *et al.* Ultrasonic metamaterials with negative modulus. *Nat. Mater.* **5,** 452–6 (2006).

2. Guenneau, S., Movchan, A., Pétursson, G. & Anantha Ramakrishna, S. Acoustic metamaterials for sound focusing and confinement. *New J. Phys.* **9,** 399–399 (2007).

3. Smith, D., Padilla, W., Vier, D., Nemat-Nasser, S. & Schultz, S. Composite medium with simultaneously negative permeability and permittivity. *Phys. Rev. Lett.* **84,** 4184–7 (2000).

4. Chen, G. Thermal conductivity and ballistic-phonon transport in the cross-plane direction of superlattices. *Phys. Rev. B* **57,** 14958–14973 (1998).

5. Zen, N., Puurtinen, T. a., Isotalo, T. J., Chaudhuri, S. & Maasilta, I. J. Engineering thermal conductance using a two-dimensional phononic crystal. *Nat. Commun.* **5,** 1–9 (2014).

6. Yang, L., Yang, N. & Li, B. Reduction of thermal conductivity by nanoscale 3D phononic crystal. *Sci. Rep.* **3,** 1143 (2013).

7. Hopkins, P. E. *et al.* Criteria for Cross-Plane Dominated Thermal Transport in Multilayer Thin Film Systems During Modulated Laser Heating. *J. Heat Transfer* **132,** 081302 (2010).

8. Sigalas, M. M. & García, N. Theoretical study of three dimensional elastic band

gaps with the finite-difference time-domain method. *J. Appl. Phys.* **87,** 3122 (2000).

9. Vasseur, J., Deymier, P., Djafari-Rouhani, B., Pennec, Y. & Hladky-Hennion, a-C. Absolute forbidden bands and waveguiding in two-dimensional phononic crystal plates. *Phys. Rev. B* **77,** 085415 (2008).

10. Torres, M., Espinosa, F. R. M. De, Garcı, D. & Garcı, N. Sonic Band Gaps in Finite Elastic Media : Surface States and Localization Phenomena in Linear and Point Defects. *Phys. Rev. Lett.* **82,** 3054–3057 (1999).

11. Kafesaki, M., Sigalas, M. M. & García, N. Frequency modulation in the transmittivity of wave guides in elastic-wave band-gap materials. *Phys. Rev. Lett.* **85,** 4044–7 (2000).

12. V. Narayanamurti, H. L. Stormer, M. A. Chin, A. C. Gossard, W. W. Selective Transmission of High-Frequency Phonons by supperlattice: The 'Dielectric' Phonon Filter. *Phys. Rev. Lett.* **2,** 2012 (1979).

13. Sigalas, M. M. & Economou, E. N. Elastic and acoustic wave band structure. *J. sound vib* **158,** 377 (1992).

14. Montero de Espinosa, F., Jiménez, E. & Torres, M. Ultrasonic Band Gap in a Periodic Two-Dimensional Composite. *Phys. Rev. Lett.* **80,** 1208–1211 (1998).

15. Vasseur, J. *et al.* Experimental and Theoretical Evidence for the Existence of Absolute Acoustic Band Gaps in Two-Dimensional Solid Phononic Crystals. *Phys. Rev. Lett.* **86,** 3012–3015 (2001).

16. Campbell, C. K. Applications of surface acoustic and shallow bulk acoustic wave devices. *Proc. IEEE* **77,** 1989 (1989).

17. Josse, F., Bender, F. & Cernosek, R. W. Sensors for Chemical and Biochemical Detection in Liquids. *Society* **73,** 5937–5944 (2004).

18. Loebl, H. P. *et al.* RF Bulk Acoustic Wave Resonators and Filters. *J. Electroceramics* **12,** 109–118 (2004).

19. J. D. Joannopoulos, R. D. Meade, and J. N. W. *Molding the Flow of Light, Princeton, NJ: Princeton University Press, 1995.* (1995).

20. Russell, P. Photonic crystal fibers. *Science* **299,** 358–62 (2003).

21. Mekis, a *et al.* High Transmission through Sharp Bends in Photonic Crystal Waveguides. *Phys. Rev. Lett.* **77,** 3787–3790 (1996).

22. Akahane, Y., Asano, T. & Song, B. High- Q photonic nanocavity in a two-dimensional photonic crystal. **425,** 4–7 (2003).

23. Lakin, K. M. Thin film resonator technology. *IEEE Trans. Ultrason. Ferroelectr. Freq. Control* **52,** 707–16 (2005).

24. Brand, B. O. Microsensor Integration Into. **94,** (2006).

25. M. Hikita, T. Tabuchi, and A. S. Miniaturized SAW devices for radio communication transceivers. *IEEE Trans. Veh. Technol.* **38,** 2–8 (1989).

26. Cady, W. G. Proceedings of the IRE. in **10,** 1922 (1922).

27. Kee, C.-S., Kim, J.-E., Park, H. Y., Chang, K. J. & Lim, H. Essential role of impedance in the formation of acoustic band gaps. *J. Appl. Phys.* **87,** 1593 (2000).

28. Hsiao, F.-L. *et al.* Complete band gaps and deaf bands of triangular and honeycomb water-steel phononic crystals. *J. Appl. Phys.* **101,** 044903 (2007).

29. Yang, S. *et al.* Ultrasound Tunneling through 3D Phononic Crystals. *Phys. Rev. Lett.* **88,** 104301 (2002).

30. Iii, R. H. O. *et al.* Ultra High Frequency (UHF) Phononic Crystal Devices Operating in Mobile Communication Bands. 1150–1153 (2009).

31. El-Kady, I., Olsson, R. H. & Fleming, J. G. Phononic band-gap crystals for radio frequency communications. *Appl. Phys. Lett.* **92,** 233504 (2008).

32. Benchabane, S., Khelif, a., Rauch, J.-Y., Robert, L. & Laude, V. Evidence for complete surface wave band gap in a piezoelectric phononic crystal. *Phys. Rev. E* **73,** 065601 (2006).

33. Cho, Y. & Rose, J. L. An elastodynamic hybrid boundary element study for elastic guided wave interactions with a surface breaking defect. *Int. J. Solids*

Struct. **37,** 4103–4124 (2000).

34. G.J. Tango, M.F. Werby, H. S. Global matrix formulation of wave phenomena in plane layered media. *Math. Model.* **8,** 450–456 (1987).

35. Tanaka, Y. & Tamura, S. Surface acoustic waves in two-dimensional periodic elastic structures. *Phys. Rev. B* **58,** 7958–7965 (1998).

36. Alaie, S., Su, M. F., Goettler, D. F., El-Kady, I. & Leseman, Z. Effects of flexural and extensional excitation modes on the transmission spectrum of phononic crystals operating at gigahertz frequencies. *J. Appl. Phys.* **113,** 103513 (2013).

37. Yao, Z.-J., Yu, G.-L., Wang, Y.-S. & Shi, Z.-F. Propagation of bending waves in phononic crystal thin plates with a point defect. *Int. J. Solids Struct.* **46,** 2571–2576 (2009).

38. J. Lourtioz, H. Benisty, V. Berger, J. Gerard, D. Maystre, and A. T. *Photonic crystals: Towards nanoscale photonic devices*. (Springer Berlin Heidelberg, 2005). doi:10.1007/3-540-27701-3

39. Baboly, M. G. *et al.* Enhanced plane wave expansion analysis for the band structure of bulk modes in two-dimensional high-contrast solid–solid phononic crystals. *Photonics Nanostructures - Fundam. Appl.* **12,** 487–492 (2014).

40. Baboly, M. G. *et al.* The effect of stiffness and mass on coupled oscillations in a phononic crystal. *AIP Adv.* **3,** 112121 (2013).

41. Wu, T.-T., Wu, L.-C. & Huang, Z.-G. Frequency band-gap measurement of two-dimensional air/silicon phononic crystals using layered slanted finger interdigital transducers. *J. Appl. Phys.* **97,** 094916 (2005).

42. Ziaei-Moayyed, M., Su, M. F., Reinke, C., El-Kady, I. F. & Olsson III, R. H. Silicon Carbide Phononic Crystal Cavities for Micromechanical Resonators. in *IEEE MEMS* 1377–1381 (2011).

43. Soliman, Y. M. *et al.* Effects of release holes on microscale solid–solid phononic crystals. *Appl. Phys. Lett.* **97,** 081907 (2010).

44. Mohammadi, S., Eftekhar, A. A., Khelif, A., Hunt, W. D. & Adibi, A. Evidence of large high frequency complete phononic band gaps in silicon phononic crystal plates. *Appl. Phys. Lett.* **92,** 221905 (2008).

45. Amir H Safavi-Naeini & Oskar Painter. Design of Optomechanical Cavities and Waveguides on a Simultaneous Bandgap. *Opt. Express* **18,** 14926–14943 (2010).

46. Soliman, Y. M. *et al.* Phononic crystals operating in the gigahertz range with extremely wide band gaps. *Appl. Phys. Lett.* **97,** 193502 (2010).

47. Kuo, N.-K. & Piazza, G. Ultra high frequency air/aluminum nitride fractal phononic crystals. *2011 Jt. Conf. IEEE Int. Freq. Control Eur. Freq. Time Forum Proc.* 1–4 (2011). doi:10.1109/FCS.2011.5977313

48. Kuo, N.-K., Zuo, C. & Piazza, G. Microscale inverse acoustic band gap structure in aluminum nitride. *Appl. Phys. Lett.* **95,** 093501 (2009).

49. Kuo, N.-K. & Piazza, G. Evidence of acoustic wave focusing in a microscale 630 MHz Aluminum Nitride phononic crystal waveguide. *2010 IEEE Int. Freq. Control Symp.* 530–533 (2010). doi:10.1109/FREQ.2010.5556274

50. Wang, Q., Quek, S. T. & Varadan, V. K. Analytical Solution for Shear Horizontal Wave Propagation in Piezoelectric Coupled Media by Interdigital Transducer. *J. Appl. Mech.* **72,** 341 (2005).

51. Search, H. *et al.* Love waves in piezoelectric coupled solid. *Smart Mater. Struct. 10* **10,** 380–388 (2001).

52. White, R. M. Acoustic sensors for physical, Chemical and Biochemical Applications. in *IEEE International Frequency control symposium* 587–594 (1998).

53. Wang, Q. Axi-symmetric wave propagation in a cylinder coated with a piezoelectric layer. *Int. J. Solids Struct.* **39,** 3023–3037 (2002).

54. Tua, P. S., Quek, S. T. & Wang, Q. Detection of cracks in cylindrical pipes and plates using piezo-actuated Lamb waves. *Smart Mater. Struct.* **14,** 1325–1342 (2005).

55. Quek, S. T., Wang, Q., Zhang, L. & Ong, K. H. Practical issues in the detection of damage. *Smart Mater. Struct* **1009,** 1009–1017 (2005).

56. M. S. Kushwaha, P. Halevi, L. Dobrzynski, and B. D.-R. Acoustic band structure of periodic elastic composites. *Phys. Rev. Lett.* **71,** 2022–2025 (1991).

57. Su, M. F., Olsson, R. H., Leseman, Z. C. & El-Kady, I. Realization of a phononic crystal operating at gigahertz frequencies. *Appl. Phys. Lett.* **96,** 053111 (2010).

58. Zhao, X. 'George' & Rose, J. L. Boundary element modeling for defect characterization potential in a wave guide. *Int. J. Solids Struct.* **40,** 2645–2658 (2003).

59. Raghavan, A. & Cesnik, C. E. S. Finite-dimensional piezoelectric transducer modeling for guided wave based structural health monitoring. *Smart Mater. Struct.* **14,** 1448–1461 (2005).

60. Olsson, R. H., El-Kady, I. F., Su, M. F., Tuck, M. R. & Fleming, J. G. Microfabricated VHF acoustic crystals and waveguides. *Sensors Actuators A Phys.* **145-146,** 87–93 (2008).

61. J. D. Achenbach, H. A. Lauwerier, W. T. K. *Wave Propagation in Elastic Solids.* (1984).

62. Sun, J. H. & Wu, T. T. A lamb wave source based on the resonant cavity of phononic-crystal plates. *IEEE Trans. Ultrason. Ferroelectr. Freq. Control* **56,** 121–128 (2009).

63. Mohammadi, S., Eftekhar, A. A., Hunt, W. D. & Adibi, A. High-Q micromechanical resonators in a two-dimensional phononic crystal slab. *Appl. Phys. Lett.* **94,** 051906 (2009).

64. Liu, V. & Fan, S. Compact bends for multi-mode photonic crystal waveguides with high transmission and suppressed modal crosstalk. *Opt. Express* **21,** 8069–75 (2013).

65. J. O. Vasseur, B. Djafari-Rouhani, L. Dobrzynski, M. S. Kushwaha, and P. H. Complete acoustic band gaps i n periodic fibre reinforced composite materials: the carbodepoxy composite and some metallic systems. *Phys.: Condes. Matter* 8759–8770 (1994).

66. Khelif, A., Choujaa, A., Benchabane, S., Djafari-Rouhani, B. & Laude, V. Guiding and bending of acoustic waves in highly confined phononic crystal waveguides. *Appl. Phys. Lett.* **84,** 4400 (2004).

67. Goettler, D. *et al.* Realizing the frequency quality factor product limit in silicon via compact phononic crystal resonators. *J. Appl. Phys.* **108,** 084505 (2010).

68. Chan, J., Eichenfield, M., Camacho, R. & Painter, O. Optical and mechanical design of a ‘ zipper ’ photonic crystal optomechanical cavity Abstract : **17,** 555–560 (2009).

69. Reinke, C. M., Su, M., Ziaei-moayyed, M., Iii, R. H. O. & El-Kady, I. F. Investigation of Full Bandgaps in Silicon Phononic Crystal Membranes with Tungsten and Air Inclusions. in *2010 IEEE International Ultrasonics Symposium* 519–522 (2010).

70. Mohammadi, S., Eftekhar, A. A., Khelif, A., Hunt, W. D. & Adibi, A. Evidence of large high frequency complete phononic band gaps in silicon phononic crystal plates. *Appl. Phys. Lett.* **92,** 221905 (2008).

71. Reinke, C. M., Su, M. F., Olsson, R. H. & El-Kady, I. Realization of optimal bandgaps in solid-solid, solid-air, and hybrid solid-air-solid phononic crystal slabs. *Appl. Phys. Lett.* **98,** 061912 (2011).

72. Mohammadi, S., Eftekhar, A. a., Pourabolghasem, R. & Adibi, A. Simultaneous high-Q confinement and selective direct piezoelectric excitation of flexural and extensional lateral vibrations in a silicon phononic crystal slab resonator. *Sensors Actuators A Phys.* **167,** 524–530 (2011).

73. Sun, J.-H. & Wu, T.-T. Propagation of surface acoustic waves through sharply bent two-dimensional phononic crystal waveguides using a finite-difference time-domain method. *Phys. Rev. B* **74,** 174305 (2006).

74. Eichenfield, M., Camacho, R., Chan, J., Vahala, K. J. & Painter, O. A picogram- and nanometre-scale photonic-crystal optomechanical cavity. *Nature* **459,** 550–5 (2009).

75. Kushwaha, M. S., Halevi, P., Dobrzynski, L. & Djafari-Rouhani, B. Acoustic band structure of periodic elastic composites. *Phys. Rev. Lett.* **71,** 2022–2025 (1993).

76. Lin, S.-C. S., Tittmann, B. R., Sun, J.-H., Wu, T.-T. & Huang, T. J. Acoustic beamwidth compressor using gradient-index phononic crystals. *J. Phys. D. Appl. Phys.* **42,** 185502 (2009).

77. Khelif, A., Djafari-Rouhani, B., Vasseur, J. O. & Deymier, P. A. Transmission and dispersion relations of perfect and defect-containing waveguide structures in phononic band gap materials. *Phys. Rev. B* **68,** 24302 (2003).

78. Olsson, R. H. III & El-Kady, I. Microfabricated phononic crystal devices and applications. *Meas. Sci. Technol.* **20,** 1–13 (2009).

79. Sriram, P., Craig, J. I. & Hanagud, S. A scanning laser doppler vibrometer for modal analysis. *Int. J. Anal. Exp. Modal Anal.* **5,** 919–925 (1990).

80. Khawar Abbas, Seyedhamidreza Alaie, Mani Hossein-Zadeh, Z. C. L. USE OF RADIATION PRESSURE TO CALIBRATE SUB MICRO-NEWTON FORCES AND DAMPING RATIOS. in *ASME Micro-ElectroMechanical Systems (MEMS) 2010, IMECE2010-38934* (2010).

Appendices

APPENDIX 1 PNC DISPERSION RELATION EIGEN FREQUENCY CODE

```
import com.comsol.model.*
import com.comsol.model.util.*

ModelUtil.showProgress(true);
model = ModelUtil.create('Model');

model.modelPath('C:\Users\Hosein\Desktop\al\Al');

model.name('model_1.mph');

a = 8e-3;     % unit is meter
r1 = 0.48*a;
t1 = 0.5*a;
kx = 0;
ky = 0;

model.param.set('a', '8e-3');
model.param.set('r1', '0.48*a');
model.param.set('t1', '0.5*a');
model.param.set('kx', '0');
model.param.set('ky', '0');

model.modelNode.create('mod1');
```

```
model.geom.create('geom1', 3);
model.geom('geom1').geomRep('comsol');
model.geom('geom1').feature.create('blk1', 'Block');
model.geom('geom1').feature.create('cyl1', 'Cylinder');
model.geom('geom1').feature.create('dif1', 'Difference');
model.geom('geom1').feature('blk1').set('size', {'a' 'a' 't1'});
model.geom('geom1').feature('cyl1').set('pos', {'a/2' 'a/2' '0'});
model.geom('geom1').feature('cyl1').set('r', 'r1');
model.geom('geom1').feature('cyl1').set('h', 't1');
model.geom('geom1').feature('dif1').selection('input').set({'blk1'});
model.geom('geom1').feature('dif1').selection('input2').set({'cyl1'});
model.geom('geom1').run;

model.view('view1').light.create('lgt4', 'DirectionalLight');

model.material.create('mat1');
model.material('mat1').propertyGroup.create('Enu', 'Young''s modulus and Poisson''s ratio');

model.physics.create('solid', 'SolidMechanics', 'geom1');
model.physics('solid').feature.create('constr1', 'PointwiseConstraint', 2);
model.physics('solid').feature('constr1').selection.set([10]);
model.physics('solid').feature.create('constr2', 'PointwiseConstraint', 2);
model.physics('solid').feature('constr2').selection.set([10]);
```

```
model.physics('solid').feature.create('constr3', 'PointwiseConstraint', 2);
model.physics('solid').feature('constr3').selection.set([10]);
model.physics('solid').feature.create('constr4', 'PointwiseConstraint', 2);
model.physics('solid').feature('constr4').selection.set([5]);
model.physics('solid').feature.create('constr5', 'PointwiseConstraint', 2);
model.physics('solid').feature('constr5').selection.set([5]);
model.physics('solid').feature.create('constr6', 'PointwiseConstraint', 2);
model.physics('solid').feature('constr6').selection.set([5]);

model.mesh.create('mesh1', 'geom1');
model.mesh('mesh1').feature.create('ftri1', 'FreeTri');
model.mesh('mesh1').feature('ftri1').selection.set([4]);
model.mesh('mesh1').feature('ftri1').feature.create('size1', 'Size');
model.mesh('mesh1').feature.create('swe1', 'Sweep');
model.mesh('mesh1').feature('swe1').feature.create('size1', 'Size');

model.cpl.create('linext1', 'LinearExtrusion', 'geom1');
model.cpl('linext1').selection.geom('geom1', 2);
model.cpl('linext1').selection.set([1]);
model.cpl.create('linext2', 'LinearExtrusion', 'geom1');
model.cpl('linext2').selection.geom('geom1', 2);
model.cpl('linext2').selection.set([2]);

model.view('view1').light('lgt1').set('intensity', '0.5');
model.view('view1').light('lgt1').set('cameracoord', false);
```

```
model.view('view1').light('lgt1').set('lightdirection', '-(-1) -(1) -(-1) ');
model.view('view1').light('lgt2').set('intensity', '0.5');
model.view('view1').light('lgt2').set('cameracoord', false);
model.view('view1').light('lgt2').set('lightdirection', '-(1) -(-1) -(1) ');
model.view('view1').light('lgt3').set('intensity', '0.5');
model.view('view1').light('lgt3').set('cameracoord', false);
model.view('view1').light('lgt3').set('lightdirection', '-(1) -(1) -(-1) ');
model.view('view1').light('lgt4').set('lightdirection', '-(-1) -(-1) -(1) ');

model.material('mat1').name('Al');
model.material('mat1').propertyGroup('def').set('electricconductivity', {'35.5e6[S/m]' '0' '0' '0' '35.5e6[S/m]' '0' '0' '0' '35.5e6[S/m]'});
model.material('mat1').propertyGroup('def').set('thermalexpansioncoefficient', {'23.1e-6[1/K]' '0' '0' '0' '23.1e-6[1/K]' '0' '0' '0' '23.1e-6[1/K]'});
model.material('mat1').propertyGroup('def').set('heatcapacity', '904[J/(kg*K)]');
model.material('mat1').propertyGroup('def').set('density', '2700[kg/m^3]');
model.material('mat1').propertyGroup('def').set('thermalconductivity', {'237[W/(m*K)]' '0' '0' '0' '237[W/(m*K)]' '0' '0' '0' '237[W/(m*K)]'});
model.material('mat1').propertyGroup('Enu').set('youngsmodulus', '70.0e9[Pa]');
model.material('mat1').propertyGroup('Enu').set('poissonsratio', '0.35');

model.physics('solid').feature('constr1').set('constraintType', 'userDefined');
model.physics('solid').feature('constr1').set('constraintExpression', 'linext1(u)-u*exp(i*kx*a)');
```

```
model.physics('solid').feature('constr1').set('constraintForce',
'test(linext1(u)*exp(i*kx*a)-u)');
model.physics('solid').feature('constr2').set('constraintType', 'userDefined');
model.physics('solid').feature('constr2').set('constraintExpression', 'linext1(v)-
v*exp(i*kx*a)');
model.physics('solid').feature('constr2').set('constraintForce',
'test(linext1(v)*exp(i*kx*a)-v)');
model.physics('solid').feature('constr3').set('constraintType', 'userDefined');
model.physics('solid').feature('constr3').set('constraintExpression', 'linext1(w)-
w*exp(i*kx*a)');
model.physics('solid').feature('constr3').set('constraintForce',
'test(linext1(w)*exp(i*kx*a)-w)');
model.physics('solid').feature('constr4').set('constraintType', 'userDefined');
model.physics('solid').feature('constr4').set('constraintExpression', 'linext2(u)-
u*exp(i*ky*a)');
model.physics('solid').feature('constr4').set('constraintForce',
'test(linext2(u)*exp(i*ky*a)-u)');
model.physics('solid').feature('constr5').set('constraintType', 'userDefined');
model.physics('solid').feature('constr5').set('constraintExpression', 'linext2(v)-
v*exp(i*ky*a)');
model.physics('solid').feature('constr5').set('constraintForce',
'test(linext2(v)*exp(i*ky*a)-v)');
model.physics('solid').feature('constr6').set('constraintType', 'userDefined');
model.physics('solid').feature('constr6').set('constraintExpression', 'linext2(w)-
w*exp(i*ky*a)');
```

```
model.physics('solid').feature('constr6').set('constraintForce',
'test(linext2(w)*exp(i*ky*a)-w)');

model.mesh('mesh1').feature('size').set('hauto', 2);
model.mesh('mesh1').feature('ftri1').feature('size1').set('hmax', '2.5E-6');
model.mesh('mesh1').feature('ftri1').feature('size1').set('hmin', '0.85E-7');
model.mesh('mesh1').feature('ftri1').feature('size1').set('hcurve', '0.3');
model.mesh('mesh1').feature('ftri1').feature('size1').set('hcurveactive', false);
model.mesh('mesh1').feature('ftri1').feature('size1').set('hnarrow', '4');
model.mesh('mesh1').feature('ftri1').feature('size1').set('hgrad', '1.35');
model.mesh('mesh1').feature('ftri1').feature('size1').set('hgradactive', false);
model.mesh('mesh1').feature('ftri1').feature('size1').set('hauto', '2');
model.mesh('mesh1').feature('ftri1').feature('size1').set('hmax', '2.5E-6');
model.mesh('mesh1').feature('ftri1').feature('size1').set('hmin', '0.85E-7');
model.mesh('mesh1').feature('ftri1').feature('size1').set('hcurveactive', false);
model.mesh('mesh1').feature('ftri1').feature('size1').set('hnarrow', '4');
model.mesh('mesh1').feature('ftri1').feature('size1').set('hgradactive', false);
model.mesh('mesh1').feature('swe1').feature('size1').set('hauto', 3);
model.mesh('mesh1').run;

model.cpl('linext1').selection('srcvertex1').geom('geom1', 0);
model.cpl('linext1').selection('srcvertex1').set([3]);
model.cpl('linext1').selection('srcvertex2').geom('geom1', 0);
model.cpl('linext1').selection('srcvertex2').set([4]);
model.cpl('linext1').selection('srcvertex3').geom('geom1', 0);
```

```
model.cpl('linext1').selection('srcvertex3').set([2]);

model.cpl('linext1').selection('srcvertex4').geom('geom1', 0);

model.cpl('linext1').selection('srcvertex4').set([1]);

model.cpl('linext1').selection('dstvertex1').geom('geom1', 0);

model.cpl('linext1').selection('dstvertex1').set([15]);

model.cpl('linext1').selection('dstvertex2').geom('geom1', 0);

model.cpl('linext1').selection('dstvertex2').set([16]);

model.cpl('linext1').selection('dstvertex3').geom('geom1', 0);

model.cpl('linext1').selection('dstvertex3').set([14]);

model.cpl('linext1').selection('dstvertex4').geom('geom1', 0);

model.cpl('linext1').selection('dstvertex4').set([13]);

model.cpl('linext2').selection('srcvertex1').geom('geom1', 0);

model.cpl('linext2').selection('srcvertex1').set([1]);

model.cpl('linext2').selection('srcvertex2').geom('geom1', 0);

model.cpl('linext2').selection('srcvertex2').set([2]);

model.cpl('linext2').selection('srcvertex3').geom('geom1', 0);

model.cpl('linext2').selection('srcvertex3').set([14]);

model.cpl('linext2').selection('srcvertex4').geom('geom1', 0);

model.cpl('linext2').selection('srcvertex4').set([13]);

model.cpl('linext2').selection('dstvertex1').geom('geom1', 0);

model.cpl('linext2').selection('dstvertex1').set([3]);

model.cpl('linext2').selection('dstvertex2').geom('geom1', 0);

model.cpl('linext2').selection('dstvertex2').set([4]);

model.cpl('linext2').selection('dstvertex3').geom('geom1', 0);

model.cpl('linext2').selection('dstvertex3').set([16]);
```

```
model.cpl('linext2').selection('dstvertex4').geom('geom1', 0);

model.cpl('linext2').selection('dstvertex4').set([15]);


model.study.create('std1');

model.study('std1').feature.create('eig', 'Eigenfrequency');




model.sol.create('sol1');

model.sol('sol1').study('std1');

model.sol('sol1').attach('std1');

model.sol('sol1').feature.create('st1', 'StudyStep');

model.sol('sol1').feature.create('v1', 'Variables');

model.sol('sol1').feature.create('e1', 'Eigenvalue');


model.result.create('pg1', 'PlotGroup3D');

model.result('pg1').feature.create('surf1', 'Surface');

model.result('pg1').feature('surf1').feature.create('def', 'Deform');


model.study('std1').feature('eig').set('neigs', '30');


model.sol('sol1').feature('st1').name('Compile Equations: Eigenfrequency');

model.sol('sol1').feature('st1').set('studystep', 'eig');

model.sol('sol1').feature('v1').set('control', 'eig');

model.sol('sol1').feature('e1').set('control', 'eig');
```

```
model.sol('sol1').feature('e1').set('neigs', '30');
model.sol('sol1').feature('e1').set('transform', 'eigenfrequency');
model.sol('sol1').feature('e1').set('linpmethod', 'sol');
model.sol('sol1').feature('e1').feature('aDef').set('complexfun', true);

model.result('pg1').name('Mode Shape (solid)');
model.result('pg1').feature('surf1').feature('def').set('scale', '4.0414518828964825E-7');
model.result('pg1').feature('surf1').feature('def').set('scaleactive', false);

nsol = 25;
k = 0:0.05:0.95;
K1 = pi / a * [k ones(1,length(k)+1) k(length(k):-1:2); zeros(1,length(k)) k 1
k(length(k):-1:2)];
freqs = zeros(nsol,size(K1,2));
for i=1:size(K1,2),
  stopBar = progressbar((i-1)/size(K1,2),4);
  if(stopBar) break; end
      kx = K1(1,i);
  ky = K1(2,i);

  model.param.set('kx', num2str(kx));
  model.param.set('ky', num2str(ky));

  display(['kx: ' num2str(kx*a/pi) '; ky: ' num2str(ky*a/pi)]);
```

```
  model.study('std1').feature('eig').set('neigs', nsol);
  model.sol('sol1').feature('e1').feature('aDef').set('complexfun', true);
  model.sol('sol1').runAll;
   ftemp = mphglobal(model, 'freq');
  freqs(:,i) = ftemp(1:nsol);
end
progressbar(1);
 figure;plot([k k+1 k+2],freqs);axis tight;grid;xlabel('Normalized Phase (k*a/2{\pi})');ylabel('Frequency (Hz)');title(['AlN-Vac PnC for r/a=' num2str(r1/a) ', t/a=' num2str(t1/a) ', a=' num2str(a/1)]);
```